PHYSICAL REVIEW B **83**, 144202 (2011)

Anomalous vibrational dynamics in the Mg_2Zn_{11} phase

H. Euchner,[1,10,*] M. Mihalkovič,[2] F. Gähler,[3] M. R. Johnson,[4] H. Schober,[4] S. Rols,[4] E. Suard,[4] A. Bosak,[5] S. Ohhashi,[6]
A.-P. Tsai,[6] S. Lidin,[7] C. Pay Gomez,[8] J. Custers,[9] S. Paschen,[9] and M. de Boissieu[10]
[1]*Institut für Theoretische und Angewandte Physik (ITAP), Universität Stuttgart, Pfaffenwaldring 57, 70569 Stuttgart, Germany*
[2]*Institute of Physics, Slovak Academy of Sciences, 84511 Bratislava, Slovakia*
[3]*Fakultät für Mathematik, Universität Bielefeld, 33501 Bielefeld, Germany*
[4]*Institut Laue-Langevin, Grenoble, France*
[5]*European Synchrotron Radiation Facility, Grenoble, France*
[6]*Institute of Multidisciplinary Research for Advanced Materials, Tohoku University, Sendai, Japan*
[7]*Inorganic Chemistry, Arrhenius Laboratory, Stockholm University, S-106 91 Stockholm, Sweden*
[8]*Department of Materials Chemistry, Uppsala University, SE-751 21 Uppsala, Sweden*
[9]*Institut für Festkörperphysik, TU Wien, Wiedner Hauptstraße 8-10, 1040 Wien, Austria*
[10]*Science et Ingénierie des Matériaux et Procédés, Grenoble–INP CNRS UJF, Boîte Postale 75, 38402 Saint Martin d'Hères, France*
(Received 25 September 2010; revised manuscript received 6 December 2010; published 7 April 2011)

We present a combined experimental and theoretical study of the structure and the lattice dynamics in the complex metallic alloy Mg_2Zn_{11}, by means of neutron and x-ray scattering, as well as *ab initio* and empirical potential calculations. Mg_2Zn_{11} can be seen as an intermediate step in structural complexity between the simple Laves-phase $MgZn_2$ on one side, and the complex 1/1 approximants and quasicrystals ZnMgAl and Zn(Mg)Sc on the other. The structure can be described as a cubic packing of a triacontahedron whose center is partially occupied by a Zn atom. This partially occupied site turned out to play a major role in understanding the lattice dynamics. Data from inelastic neutron scattering evidence a Van Hove singularity in the vibrational spectrum of Mg_2Zn_{11} for an energy as low as 4.5 meV, which is a unique feature for a nearly-close-packed metallic alloy. This corresponds to a gap opening at the Brillouin zone boundary and an interaction between a low-lying optical branch and an acoustic one, as could be deduced from the dispersion relation measured by inelastic x-ray scattering. Second, the measured phonon density of states exhibits many maxima, indicating strong mode interactions across the whole energy range. The origin of the low-energy modes in Mg_2Zn_{11} and other features of the vibrational spectra are studied, using both *ab initio* and empirical potential calculations. A detailed analysis of vibrational eigenmodes is presented, linking features in the vibrational spectrum to atomic motions within structural building blocks.

DOI: 10.1103/PhysRevB.83.144202 PACS number(s): 61.66.Dk

I. INTRODUCTION

Quasicrystals are complex, long-range-ordered materials that lack translation invariance, but exhibit sharp Bragg reflections in their diffraction patterns (see Refs. 1 and 2 for an introduction). Due to this lack of lattice periodicity the Bloch theorem cannot be applied, making the understanding of physical properties, like lattice dynamics, a challenging problem. Significant progress in the understanding of the atomic structure of icosahedral quasicrystals has been achieved recently thanks to the discovery of the binary CdYb quasicrystal.[3] In this system it has been shown that the structure can be described as a quasiperiodic packing of a large atomic cluster (Tsai-type cluster), which is also found in periodic approximants.[4] In the isostructural Zn(Mg)Sc, a detailed analysis of the lattice dynamics has been carried out experimentally in both the quasicrystal and its periodic 1/1 approximant.[5] Significant differences were observed and interpreted as resulting from the quasiperiodic distribution of pseudo-Brillouin-zones in the quasicrystal. Atomic scale simulations, using oscillating pair potentials, could reproduce in a quantitative way the observed inelastic scattering signal together with the differences between the quasicrystal and its 1/1 approximant. As in other quasicrystals,[6] an abrupt broadening of the acoustic excitation was observed for wave vectors of the order of the atomic cluster size, where a strong mixing between the acoustic mode and low-lying optical excitation occurs. However, the exact role played on one hand by the atomic clusters and on the other hand by the long-range periodic or quasiperiodic order remains to be elucidated. This is why we have set up a systematic study of phases of increasing complexity in the (Al-)Mg-Zn system, featuring the $MgZn_2$ Laves phase (12 atoms in the unit cell) and two phases with more complex structures, Mg_2Zn_{11} (39 atoms in the unit cell) and τ-AlMgZn (162 atoms in the unit cell).[7] In this context the Laves-phase $MgZn_2$ serves as a prototype of a simple structure. Its atomic configuration is a tetrahedrally close packing of large (Mg) and small (Zn) atoms, with characteristic Friauf polyhedra (around the Mg atoms) as structural units, this also being the constituent motif of the complex τ-phase AlMgZn. The lattice dynamics of the $MgZn_2$ Laves phase has been studied previously in experiment and simulation,[8,9] making $MgZn_2$ perfectly suitable for comparison.

This paper has its focus on the Mg_2Zn_{11} phase, which evidences structural and dynamical peculiarities from several viewpoints. Its Zn content of ~85% is close to that of pure hexagonal Zn, whose c/a ratio, equal to 1.856, departs significantly from the close-packed optimal value of 1.623. This results in the local environment of Zn being strongly distorted and different from the $MgZn_2$ close-packed structure. Instead of 12 nearest neighbors at equivalent distances as in

©2011 American Physical Society

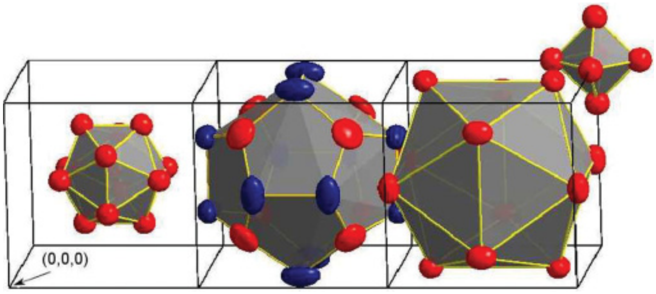

FIG. 1. (Color online) Structure of Mg_2Zn_{11} showing the constituent shells of the Pauling triacontrahedron, with Zn5 icosahedron (left), followed by a distorted dodecahedron of Mg and Zn4 atoms (middle), and a Zn3 icosahedron (right), connected by Zn2 octahedra. The view is along the *c* axis, with the *a* and *b* axes in plane. Zn atoms are represented in red (light gray), Mg atoms in blue (dark gray).

regular hcp metals, the local environment consists of six atoms at 2.664 Å and a further six atoms at 2.91 Å, leading to a stacking of hexagonal layers, which are somehow weakly "bonded," as evidenced by a soft transverse acoustic (TA) phonon branch.[10,11] The deviation from the ideal c/a ratio can be understood by investigating the electronic density of states (EDOS). Whereas the stabilization of the distorted hcp structure is attributed to a dip in the EDOS at the Fermi level, hcp Zn with an ideal c/a ratio was shown to have a significantly increased EDOS at the Fermi level, thus rendering such a configuration unstable. This dip in the EDOS seems furthermore to be responsible for the distorted hcp structure being favored as compared to the fcc structure.[12] The high Zn content in Mg_2Zn_{11} is therefore expected to have a strong impact on structural and dynamical properties of this phase.

Structurally, Mg_2Zn_{11} with its 39 atoms in the cubic unit cell, can be viewed either as a cubic packing of Pauling triacontahedra (PTRs) linked through Zn octahedra [Figs. 1 and 3(a)] , or as an embedding of icosahedra in a fcc-structure matrix [Figs. 2 and 3(b)], or even as a network of distorted and modified overlapping Tsai clusters with octahedra replacing tetrahedra in the famous binary Ca-Cd/Yb-Cd or Sc-Zn structures near the 1 : 6 Zn- (Cd-)rich composition.[13,14]

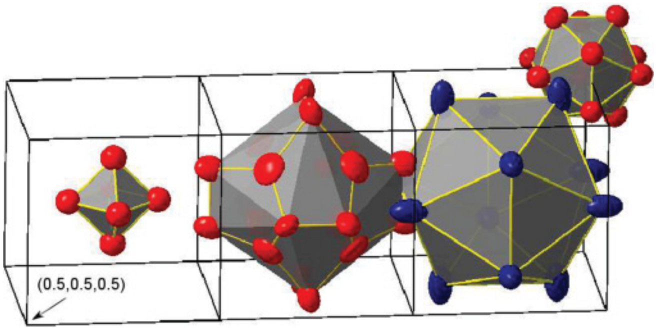

.

FIG. 2. (Color online) Structure of Mg_2Zn_{11} showing the constituent shells of the Tsai-type cluster, with Zn2 octahedron (left), strongly distorted Zn3/Zn4 dodecahedron (middle), and Mg icosahedron (right) connected by Zn5 icosahedra. The view is along the *c* axis, with the *a* and *b* axes in plane. Zn atoms are represented in red (light gray), Mg atoms in blue (dark gray).

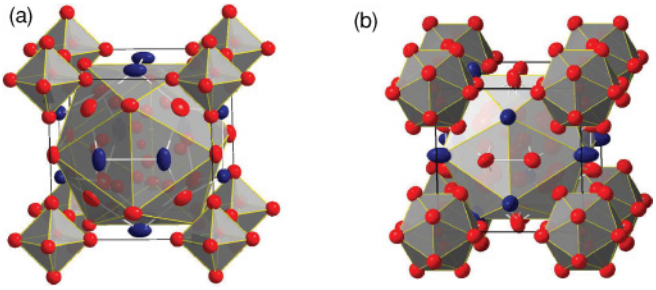

.

FIG. 3. (Color online) Structure of Mg_2Zn_{11} (a) represented as cubic packing of Pauling triacontahedral clusters linked by Zn octahedra and (b) represented as filled double icosahedral shells connected by Zn icosahedra, with Mg atoms in blue (dark gray) and Zn atoms in red (light gray). The shapes of the atoms represent the atomic displacement parameters.

The presented survey on Mg_2Zn_{11} is also motivated by the exceptional dynamical features this phase exhibits in the low-energy part of the vibrational density of states (DOS), which are investigated in detail by experiment and calculation within this study. Furthermore, the mechanisms that are responsible for these low-energy modes and other distinct features in the vibrational spectrum are discussed and interpreted in terms of atomistic motions. Finally, the influence of structural complexity on the lattice dynamics of complex metallic alloys (CMAs) is explored by using the simple $MgZn_2$ Laves phase[8] as a reference structure within this study.

II. ATOMIC STRUCTURE

A. Sample preparation

An initial alloy with the composition Mg_2Zn_{11} was prepared by an induction melting furnace and quenched afterward. It was then annealed for 170 h at 300 °C, leading to an almost single-phased Mg_2Zn_{11} sample with a few traces of Zn (less than 5%) as shown by x-ray and scanning electron microscopy (SEM) analysis. This polycrystalline sample was used for the elastic and inelastic neutron scattering experiments.

Part of the sample was further annealed for three weeks at 350 °C, in order to obtain single-grain samples of the order of 0.1 mm in diameter for the purpose of elastic and inelastic x-ray scattering experiments. From a systematic search over several samples (most of them being twinned and rather small) a single crystal with a size of the order 0.2 mm could be extracted and has been used for the x-ray structural analysis and lattice dynamics studies.

B. Structure refinement

Since the structure determination of Mg_2Zn_{11} dates back to 1949 (Ref. 15) and does not contain any information on the atomic displacement parameters (ADPs), an x-ray study was conducted with the single-crystal sample. The single-crystal data acquisition was carried out using a Kappa diffractometer. 22 957 (13 539 observed) reflections were collected in the 2θ range 4.1° to 34.5°. These reflections were averaged to 518 unique (426 observed) intensities and yielded an internal R value of 5.2 (4.9 for observed reflections). The

TABLE I. List of refined Wyckoff site positions and occupations of the Mg_2Zn_{11} structure. Space group $Pm\overline{3}$; cubic lattice parameter $a = 8.5398$ Å.

No.	Chem.	Site	Occ.	x/a	y/a	z/a
1	Zn1	$1b$	0.72	0.5	0.5	0.5
2	Zn2	$6e$	1	0.2302(3)	0	0
3	Zn3	$6g$	1	0.1625(3)	0.5	0
4	Zn4	$8i$	1	0.21821(13)	0.21821(13)	0.21821(13)
5	Zn5	$12k$	1	0.5	0.23798(17)	0.34315(19)
6	Mg	$6f$	1	0.2995(4)	0	0.5

refinement, showed furthermore that the Zn1 site (see Table I) corresponding to the central position of the Zn icosahedron inside the Pauling triacontahedron was not fully occupied by Zn atoms. Although the fraction of the partially occupied sites is small (1/39), Secs. IV A and IV C 1 discuss their significant impact on energetic stability and lattice dynamics. Because the scattering power of Mg is rather low ($Z = 12$) as compared to that of Zn ($Z = 30$), it was not possible from the x-ray experiment alone to differentiate between a Zn-Mg or a Zn-vacancy mixed occupancy at the cluster center. Since neutrons have similar scattering length for Mg ($b_{\mathrm{coh}} = 5.375$ fm) and Zn ($b_{\mathrm{coh}} = 5.680$ fm), neutron diffraction could be used to solve this ambiguity. The neutron powder spectrum was obtained at the D2B diffractometer at the Institut Laue-Langevin (ILL) with a wavelength of 1.051 Å for an angular range of $5^\circ < 2\theta < 165^\circ$. Then a Rietveld refinement of the combined neutron and x-ray data was conducted using the software JANA.[16] The results of the structure refinement are shown in Tables I and II. The corresponding R values are denoted in Table III.

The combined x-ray and neutron refinement showed that the cluster center is fractionally occupied by Zn (72% occupancy). This conclusion is also consistent with interatomic distances, since the central Zn icosahedron space is not large enough to accept a big Mg atom. As will be pointed out later in this work, the distribution of vacancies on this site exhibits, despite its small relative weight (∼1/39), a strong impact on the atomic dynamics. The other important result of this structure determination is the very large anisotropic displacement parameters, which are observed for some atoms. This is exemplified in Figs. 1 and 3(a), where large ADPs are observed for Mg and Zn atoms constituting the dodecahedron shell (see following section). In particular the Mg atoms show a tendency for linear motion, as can be seen by the cigarlike shape of the ADP ellipsoids in Fig. 1, central panel. The Zn4 atoms also have strongly anisotropic ADPs, with motions confined in planes perpendicular to the threefold axis (Fig. 1, central panel). These anisotropic ADPs are related to the loose packing of some specific sites as explained hereafter. As opposed to the structure of the $MgZn_2$ Laves phase in which Mg atoms are in 16-coordinated Friauf polyhedra and each Mg has four Mg neighbors, in Mg_2Zn_{11} their coordination is 17, and they occur in pairs encapsulated by elongated hexagonal Zn cages (Fig. 4), opening space for vibrational motions. The local environments of the constituting atoms in Mg_2Zn_{11} are depicted in Fig. 4. While the reference structure $MgZn_2$ is close packed with exclusive Frank-Kasper coordination and nearest-neighbor distances of 2.6 Å for Zn-Zn, 3.05 Å for Mg-Zn, and 3.20 Å for Mg-Mg (Table IV), in Mg_2Zn_{11} only two sites, Zn1 and Zn5, possess icosahedral coordination. The Zn3 and Zn4 sites have no Frank-Kasper coordination and evidence unusually large Zn-Zn distances of 3.08 Å(Table V). Furthermore, the unusual coordination of the Mg atoms results in anomalously long (∼3.4 Å) Mg-Zn linkages to the Zn2 and Zn3 sites; such distances do not occur in the reference structure $MgZn_2$ (see Tables IV and V). The nonideal coordination with these increased interatomic distances is also reflected in the anisotropies that Zn(3) and Zn(4) atoms evidence in their ADPs, as well as the tendency to linear motion found for the Mg atoms (see Table II).

TABLE II. Anisotropic atomic displacement parameters in Å^2 (multiplied by 10^4).

	U_{11}	U_{22}	U_{33}	U_{12}	U_{13}	U_{23}
Zn1	66(10)	66(10)	66(10)	0	0	0
Zn2	133(9)	127(10)	127(10)	0	0	0
Zn3	119(10)	212(11)	101(10)	0	0	0
Zn4	201(4)	201(4)	201(4)	−67(4)	−67(4)	−67(4)
Zn5	109(6)	121(7)	122(7)	0	0	−12(5)
Mg	183(15)	80(11)	55(2)	0	0	0

TABLE III. Results of the combined x-ray and neutron refinement, where $R(p)$, $Rw(p)$, and GOF stand for the R factor, weighted R factor, and goodness of fit for the single-crystal (powder) refinement, respectively.

Neutron	Rp	Rwp	GOF
	4.16	5.66	3.14
X-ray	R(obs/all)	Rw(obs/all)	GOF(obs/all)
	4.33/8.36	5.05/5.24	2.19/1.67

C. Structure interpretations in terms of icosahedral clusters

Mg_2Zn_{11} can be described as an intriguing cluster-based structure, combining overlapping Pauling triacontahedra (in the Frank-Kasper phases context, PTRs are the first two

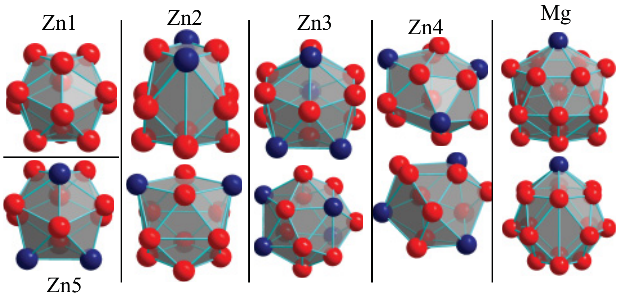

FIG. 4. (Color online) Local environment polyhedra. The polyhedra in the second row are rotated by 90° around the vertical axis with respect to the first row, except in the leftmost figures. These show the two icosahedral environments, Zn1 (top) and Zn5 (bottom). The other columns depict the Zn2, Zn3, Zn4, and Mg environments, from left to right. Zn atoms are represented in red (light gray) and Mg atoms in blue (dark gray).

TABLE IV. Coordination shells of $MgZn_2$, showing the nearest-neighbor distances. Here μ denotes the number of Mg and Zn neighbors within the given range. In the last column the coordination number of each atom is given.

	Neighbor	R (Å)	μ	Coordination
Zn1	Zn	2.62	6	
Zn1	Mg	3.04	6	12
Zn2	Zn	2.54–2.64	6	
Zn2	Mg	3.04–3.05	6	12
Mg	Zn	3.04–3.05	12	
Mg	Mg	3.17–3.20	4	16

shells of Bergman clusters, like τ-AlMgZn,[7] for example), and Tsai clusters (seen in $ScZn_6$, for example[17]) in a comparably small cubic cell.

Pauling triacontahedra. A perhaps more obvious interpretation is in terms of PTR clusters at the *body center* of the cubic unit cell, linked by Zn octahedra. The PTR consists of the fractionally occupied central Zn1 atom, which is surrounded by an icosahedral shell of Zn5 atoms. The second shell is formed by a dodecahedron consisting of eight Zn4 and twelve Mg atoms. Due to chemical ordering the icosahedral symmetry is broken, leaving this shell with cubic symmetry. The second PTR shell is completed by an almost perfect double size icosahedron of Zn3 atoms [see Figs. 1 and Fig. 3(a)]. The only atoms left out are those of the Zn2 site, which form the octahedra centered at the corners of the cell. We note that in the Bergman phases the PTR dodecahedron sites are nominally appropriate for "large" atoms; in the Mg_2Zn_{11} composition with only ~15% of Mg some of these nominally large sites have to be occupied by (smaller) Zn atoms.

Tsai cluster. An inspection of the shells around the Zn2 octahedra at the corner of the unit cell reveals the correspondence with Tsai clusters[3] found in $ScZn_6$ and related compounds,[13,14] including 1/1 and 2/1 approximants and binary or ternary quasicrystal systems (note the practically identical Zn content of ~85%), as shown on Figs. 2 and 3(a). First, the union of the Zn4 cube and 12 Zn3 atoms forms a dodecahedral shell, dimpled in eight cubic 3–threefold directions toward the cluster center (Zn4 site). (In fact, the Zn2 octahedron plus the Zn4 cube form a fcc cluster.) The Mg atoms in the second shell form a nearly perfect icosahedron with ~5 Å radius (Table VI includes the first four shells of the node cluster). Finally, the orbits Zn5 and Zn2 even form a distorted icosidodecahedron, with atoms approximately at the mid-edge positions of the Mg icosahedron. Thus, Mg_2Zn_{11} can in fact be considered as a 1/0 approximant to the aforementioned $ScZn_6$ 1/1 Tsai-cluster approximant structure. Recently, the Mg_2Zn_{11} prototype structure has been used as a starting point for quasicrystal formation by "electronic tuning."[18]

TABLE V. Coordination shells of Mg_2Zn_{11}, showing the nearest-neighbor distances. Here μ denotes the number of Mg and Zn neighbors within the given range. In the last column the coordination number of each atom is given.

	Neighbor	R (Å)	μ	Coordination
Zn1	Zn	2.61	12	12
Zn2	Zn	2.64–2.78	10	
Zn2	Mg	3.44	2	12
Zn3	Zn	2.55–2.78	5	
Zn3	Mg	2.92	2	
Zn3	Zn	3.08	4	
Zn3	Mg	3.34	2	13
Zn4	Zn	2.64	6	
Zn4	Zn	3.08	3	
Zn4	Mg	3.12	3	12
Zn5	Zn	2.55–2.75	9	
Zn5	Mg	2.92	3	12
Mg	Zn	2.92–2.97	8	
Mg	Zn	3.12–3.34	6	
Mg	Mg	3.40	1	
Mg	Zn	3.44	2	17

In Table VI, the PTR and Tsai-type cluster shells are associated with Wyckoff sites and compared to the density-functional-theory-relaxed structure (see Sec. IV). The refined structure (Sec. II B) is in good agreement with the *ab initio* calculation, much more so than the original model of Samson.[15]

III. LATTICE DYNAMICS

A. Theoretical background

The information on the lattice dynamics of a system is contained in the dynamic structure factor $S(Q,\omega)$, a quantity, which is directly measurable with inelastic neutron or x-ray scattering. The dynamic structure factor is the response function of a system and can be described in the most general representation as space-time Fourier transform of the density-density correlation function:[19]

$$S(\vec{Q},\omega) = \frac{1}{2\pi N\hbar}\int dt e^{-i\omega t}\sum_{l,m} b_l b_m \langle e^{i\vec{Q}\vec{r}_l(0)} e^{i\vec{Q}\vec{r}_m(t)}\rangle \quad (1)$$

with position vector $\vec{r}_l$, total momentum transfer $\vec{Q} = \vec{k}_f - \vec{k}_i$, energy transer $\hbar\omega = E_f - E_i$, and scattering length b_l in the case of neutron scattering. For neutron scattering $S(\vec{Q},\omega)$ can be divided into a coherent and an incoherent part, which are represented as correlation and autocorrelation functions, respectively:

$$S(\vec{Q},\omega)_{\text{coh}} = \frac{1}{2\pi N\hbar}\int dt e^{-i\omega t}\sum_{l\neq m} b_l b_m \langle e^{i\vec{Q}\vec{r}_l(0)} e^{i\vec{Q}\vec{r}_m(t)}\rangle, \quad (2)$$

$$S(\vec{Q},\omega)_{\text{inc}} = \frac{1}{2\pi N\hbar}\int dt e^{-i\omega t}\sum_{l} b_l b_l \langle e^{i\vec{Q}\vec{r}_l(0)} e^{i\vec{Q}\vec{r}_l(t)}\rangle. \quad (3)$$

If the effective atomic interaction potential is assumed to be harmonic, for purely incoherent scattering materials the following expression is valid:[19]

$$S(Q,\omega)_{\text{inc}} = \sum_{\mu=\text{Mg,Zn}} \frac{\sigma^{\mu}_{\text{inc}}}{2M_\mu} e^{-2W_\mu} Q^2 \frac{G_\mu(\omega)}{\omega}[n(\omega)+1] \quad (4)$$

with the thermal occupation factor $n(\omega,T)+1$, the incoherent scattering cross section $\sigma^{\mu}_{\text{inc}}$ of atom μ, the Debye-Waller factor W, and the partial density of states (PDOS) $G_\mu(\omega)$ of atom μ.

TABLE VI. Cluster-based interpretation of the Mg_2Zn_{11} structure. Nodes of the cubic lattice are decorated by Tsai-like clusters, centered by Zn2 octahedra. Body centers are decorated by Pauling triacontahedra whose second-shell dodecahedra are occupied by Mg and Zn atoms. The last two columns are rms displacements of the *ab initio*–relaxed atomic positions, from the positions refined against the x-ray and neutron data of the present work (dR_1) and those reported in Samson's original model (dR_2), showing the improved agreement between experiment and calculation.

Site	Shell	Node R (Å)	μ	Shell	Body center R (Å)	μ	dR_1 (Å)	dR_2 (Å)
Zn1	–	–	–	Center	0	1	0	0
Zn5	–	–	–	Icosahedron	2.61	12	0.04	0.08
Zn2	Octahedron	1.97	6	–	–	–	0.00	0.04
Zn4	Dodecahedron	3.23	8	Dodecahedron	4.17	8	0.02	0.05
Zn3	Dodecahedron	4.49	12	Icosahedron^2	5.15	12	0.00	0.00
Mg	Icosahedron	4.98	12	Dodecahedron	4.60	12	0.04	0.157

Within the above equation a quantity, closely related to the vibrational density of states, the generalized vibrational density of states (GVDOS), can be defined:

$$G(\omega) = \sum_{\mu=\mathrm{Mg,Zn}} \frac{\sigma^{\mu}_{\mathrm{inc}}}{M_\mu} e^{-2W_\mu} G_\mu(\omega). \tag{5}$$

With the PDOS representing the contribution of a certain atom to the total DOS it becomes clear from Eq. (5) that the GVDOS is to be interpreted as a weighted DOS, thus being closely related to the "real" phonon DOS, which determines, e.g., the free energy, vibrational entropy, or specific heat. The GVDOS can be obtained directly from $S(Q,\omega)$ by modifying Eq. (4) and summing over all Q:

$$G(\omega) = \sum_{Q} S(Q,\omega)_{\mathrm{inc}} \frac{2\omega}{Q^2[n(\omega,T)+1]}. \tag{6}$$

The scattering of Mg_2Zn_{11} is, however, mainly coherent, as can be seen from the coherent (incoherent) cross sections of Mg and Zn, which are 3.631 barn (0.08 barn) and 4.054 barn (0.077 barn), respectively. The average coherent structure factor, as it is obtained for a polycrystalline sample, however, can be shown to be a good approximation to the incoherent structure factor, if $\sigma^{\mu}_{\mathrm{inc}}$ is replaced by $\sigma^{\mu}_{\mathrm{coh}}$ and a large volume in reciprocal space is covered by the experiment.[20] This so-called incoherent approximation is applied in the experiments described below.

B. Inelastic neutron scattering

The first part of the experimental results on the vibrational properties of Mg_2Zn_{11} stems from an inelastic neutron scattering experiment at the IN6 time-of-flight spectrometer at the ILL. The IN6 spectrometer covers an angular range from 10° to 115°, enabling a broad range of wave vector transfer Q to be measured simultaneously. It is, however, restricted to a maximum momentum transfer of 2.6 Å^{-1} and a maximum energy gain of 200 meV. For the IN6 experiment the above-described polycrystalline sample of about 1 cm^3 size was investigated at room temperature for a total measuring time of 16 h. The spectrometer was operated in the energy gain mode, with incoming neutrons of wavelength 4.08 Å (equivalent to a neutron kinetic energy of 4.8 meV) and in high-resolution geometry, with the best resolution of 0.1 meV around 8 meV. The measured double-differential scattering cross section $\frac{d^2\sigma}{dt d\Omega}$ was converted to the energy and wave vector domain to obtain the dynamical response $S(Q,\omega)$. By use of Eq. (6) and application of an iterative correction for multiphonons the GVDOS was extracted.

In Fig. 5 the measured GVDOS of Mg_2Zn_{11} is compared to that of our reference compound, $MgZn_2$, measured for 14 h under the same experimental conditions. This comparison shows striking differences in the vibrational properties of these two close-packed Mg-Zn phases. The Laves phase shows an almost Debye behavior with an ω^2 dependence of the GVDOS intensity up to 10 meV (except for a small shoulder at 7 meV), and three pronounced peaks at higher energies. The situation is markedly different for Mg_2Zn_{11} which, as shown in Fig. 5, displays a significant departure from Debye's law and a Van Hove singularity at ∼5 meV, representing an exceptional feature for a nearly close-packed metallic alloy. In addition, more features are observed in the high-energy part of the spectrum.

In a second experiment Mg_2Zn_{11} was studied at the IN4 time-of-flight spectrometer at the ILL. The IN4 spectrometer covers scattering angles of up to 120° and was operated with a wavelength of 2.2 Å (equivalent to a neutron kinetic energy of 16.9 meV) thus making a larger Q range accesible as compared to IN6. In this setup, energy transfer of up to 12 meV on the

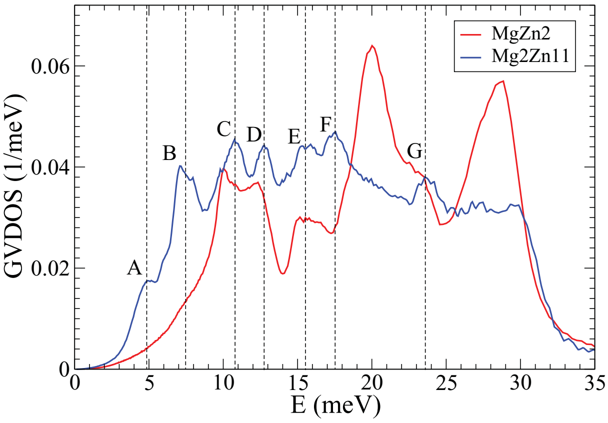

FIG. 5. (Color online) Room-temperature GVDOS from inelastic neutron scattering for Mg_2Zn_{11} [blue (dark gray line) with peak labels A to G as in Table VII] and $MgZn_2$ [red (light gray) line].

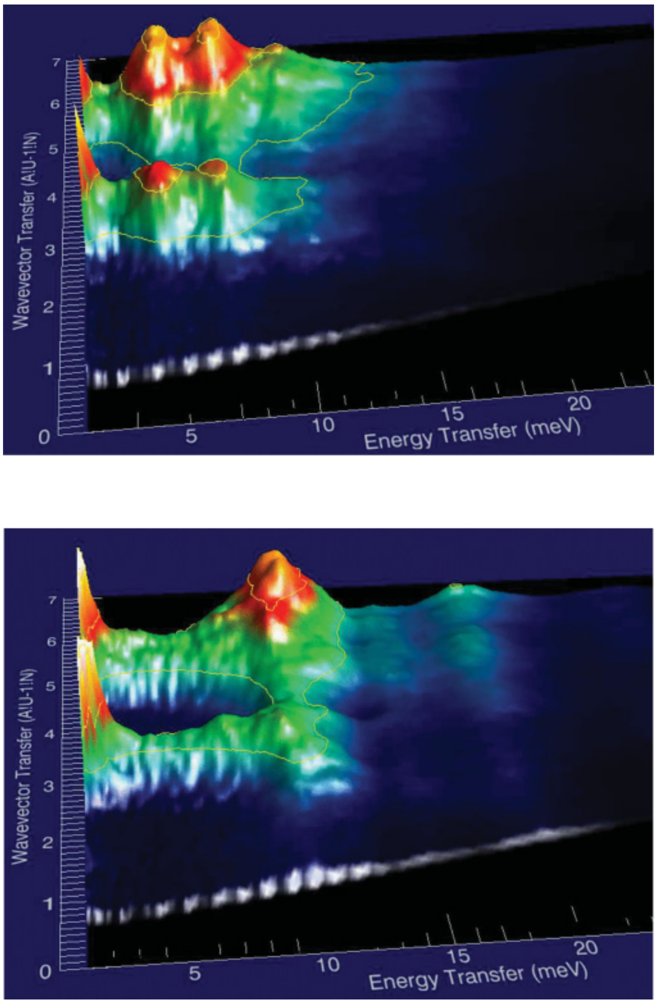

FIG. 6. (Color online) $S(Q,\omega)$ from inelastic neutron scattering for Mg_2Zn_{11} (top) and $MgZn_2$ (bottom) at 300 K.

Stokes side (energy loss) is possible, making measurements at low temperatures with resolution of 0.5 meV feasible. On the anti-Stokes side (energy gain) the IN4 spectrometer is able to investigate spectra up to 100 meV, but with lower resolution. Figure 6 displays the dynamic structure factors for Mg_2Zn_{11} and the $MgZn_2$ Laves phase (anti-Stokes side), again clearly showing the striking differences between these two phases. For $MgZn_2$, we find two strong Bragg peaks with associated acoustic modes up to an energy transfer of about 10 meV and two well-defined, dispersionless optical bands at about 20 and 29 meV. For Mg_2Zn_{11} the picture is distinctly different. Although there are two strong Bragg peaks leading to acoustic modes, they bend over at significantly lower energies, due to the occurrence of low-lying optical bands. Furthermore there is a pseudogap visible between two dispersionless excitations at 4.5 and 7 meV, respectively. In addition we see a strong localization of the intensity in wave vector Q as compared to the localization in energy ω, which is seen for the optical modes in $MgZn_2$ (Fig. 6).

From these experiments we find a behavior rather typical of a simple crystal for $MgZn_2$, whereas the more complex Mg_2Zn_{11} phase exhibits extraordinary features in the low-energy range. The low-energy excitations observed in the Mg_2Zn_{11} spectrum may be related to "weakly" bonded atoms at certain sites, therefore making them susceptible to showing anharmonic behavior. To verify the character of these low-energy excitations, the dynamic structure factor was studied on the IN4 spectrometer for different temperatures with exposure times of at least 4 h each. In the case of anharmonicity, one expects a change of position and width of the excitation with variation of temperature T. Indeed, we do observe changes in $S(Q,\omega)$ and GVDOS with decreasing temperature, however, mostly at high energies. As a general trend (see Fig. 7), the peaks observed in the GVDOS are broadened as T is increased. Moreover the high-energy part around 30 meV exhibits a pronounced decrease in intensity (see Fig. 7, which compares the spectra measured at 100 and 300 K).

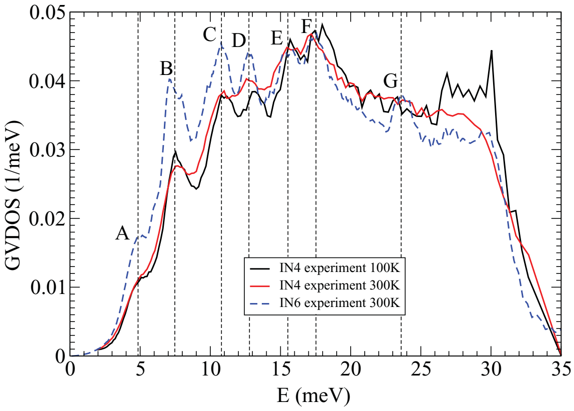

.

FIG. 7. (Color online) GVDOS from inelastic neutron scattering for Mg_2Zn_{11} at temperatures of $T = 100$ K (black line) and 300 K [red (light gray line)], IN4 data. Room temperature IN6 data with peak labels (Table VII) are shown for reference [dashed blue (gray) line].

To investigate more closely the temperature dependence of the low-energy part of the spectrum, the integrated intensity $[\int S(Q,\omega)dQ]$ was extracted for feature-rich intervals in reciprocal space. In Fig. 8, the integral $\int S(Q,\omega)dQ$, with a Q range from 3.25 to 3.75 Å^{-1}, is depicted for energy loss setup at five different temperatures. The resulting peaks were fitted with Gaussian functions (see Table VIII), showing also only slight changes with temperature. From these fits we conclude that the peak B at around 7 meV is slightly shifted to lower energies with increasing temperature, indicating a weakly anharmonic character. The peak A at around 4.5 meV shows a bigger uncertainty in its position, but the energy appears to stay constant over the investigated temperature range. Thus, anharmonic effects in the low-energy part of the Mg_2Zn_{11} spectrum are negligible.

An appreciable anharmonic effect is visible for the intermediate-energy peak D at ~13 meV (see Table VII for peak labels): Its energy obtained in both the IN4 and the IN6 experiments exactly coincides at 300 K, whereas it lies ~0.5 meV higher for the IN4 measurement at 100 K. This effect is certainly not quasiharmonic, since both lower- (C) and higher- (E) energy peaks have essentially the same energies at both temperatures. Interestingly, this peak is mainly due to the Zn5 icosahedron vibration, and its height and energy are

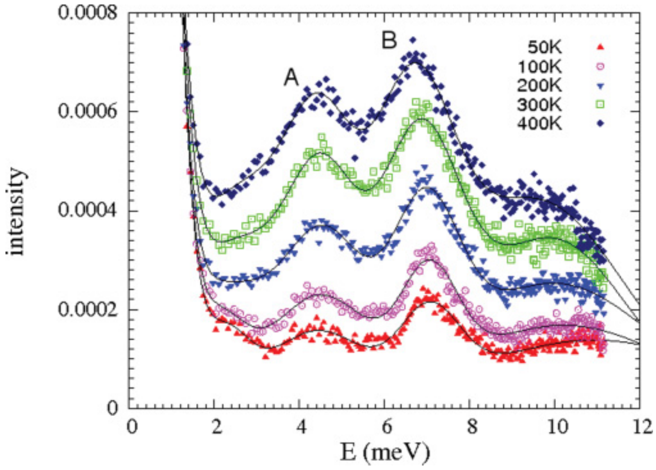

FIG. 8. (Color online) Intensity distribution of the Q-integrated $S(Q,\omega)$ data as a function of energy for Mg_2Zn_{11} (integrated Q range 2.75 to 3.25 Å^{-1}), at different temperatures for neutron energy loss. The solid curves are fits to the experimental data.

extremely sensitive to the fractional occupancy of the Zn1 site (see Sec. IV E).

As a side effect, we found that the intensity distribution in the experimental GVDOS, especially around 7 meV, is different in the IN4 measurement as compared to the IN6 one. This stems from the different (Q,ω) range accessible with the two spectrometers. This hypothesis is confirmed by the almost identical intensity distribution when using the same (Q,ω) range to compute the GVDOS from IN4 and IN6 data, respectively. This points to the known limitations of the so-called incoherent approximation when the scattering is essentially coherent, as it is in our case. Furthermore, if a detailed intensity comparison is to be carried out, the necessity of using a well-sampled (Q,ω) range becomes evident for simulating the GVDOS.[21]

C. Inelastic x-ray scattering

Since Mg_2Zn_{11} single crystals big enough for neutron scattering experiments could not be grown, inelastic x-ray measurements were conducted on a small sample at the ESRF beamline ID28. The dynamic structure factor [Eq. (1) with x-ray form factor instead of neutron scattering length] was measured as a function of energy for constant values of $\vec{Q}$ in distinct directions of reciprocal space (see Fig. 12). For our purpose, the (11,11,11) reflection of a Si monochromator was used to select an incoming energy of 21.747 keV enabling a total energy resolution of 1.5 meV full width at half maximum (FWHM). The momentum transfer was selected by an appropriate choice of scattering angle and sample orientation, with the in-plane momentum resolution being ∼0.034 Å^{-1} whereas the out-of-plane momentum resolution was ∼0.1 Å^{-1}. The measurements focused on identifying the low energy modes and therefore, the scans were restricted to an energy range from 0-15 meV. The dynamic response function $S(Q,\omega)$ has been measured for different high-symmetry directions around strong Bragg reflections. A proper choice of the measurement geometry allows for the selection of particular acoustic modes [see Eqs. (7) and (8)]. The TA modes have been measured around the Bragg peaks (0,8,0) and (0,4,0) for phonon wave vectors $\vec{q}$ propagating along (1,0,0) and (1,1,−1). For the TA modes propagating along the (1,0,0) direction, we observe a very limited region for which an almost linear dispersion is obeyed (see Fig. 9). Rapidly the dispersion bends over and a gap opens at the Brillouin zone boundary. This is exemplified in Fig. 10, which shows an energy scan recorded at the Brillouin zone boundary (top panel): the two excitations located at 3.5 and 5.5 meV are clearly identified, in good agreement with the powder averaged $S(Q,\omega)$ scattering function observed by inelastic neutron scattering (see Fig. 5). The gap width is of the order of 2 meV. At the same time, we observe a broad dispersionless opticlike excitation located at 11 meV. We have also analyzed the width and normalized integrated intensity (for details see Ref. 5) of the acoustic excitation. Although the experimental results are a bit noisy, we observe a broadening

TABLE VII. Pronounced peaks in the GVDOS of Mg_2Zn_{11}. The labels A to G are assigned to the peak energies.

Peak	*A*	*B*	*C*	*D*	*E*	*F*	*G*
E (meV)	4.9	7.4	10.8	12.7	15.6	17.4	23.6

TABLE VIII. Positions and full widths at half maximum (FWHM) of the peaks in the integrated intensity (range 2.75 to 3.25 Å^{-1}) of Mg_2Zn_{11} as a function of temperature, from the IN4 spectrometer.

T (K)	*E* (meV)	*dE* (meV)	FWHM (meV)	*E* (meV)	*dE* (meV)	FWHM (meV)
50	4.38	0.07	3.13	7.06	0.03	1.15
100	4.44	0.06	3.33	7.06	0.02	1.03
200	4.60	0.23	2.21	6.95	0.04	1.44
300	4.54	0.15	1.68	6.80	0.04	2.07
400	4.49	0.20	1.62	6.62	0.06	2.09

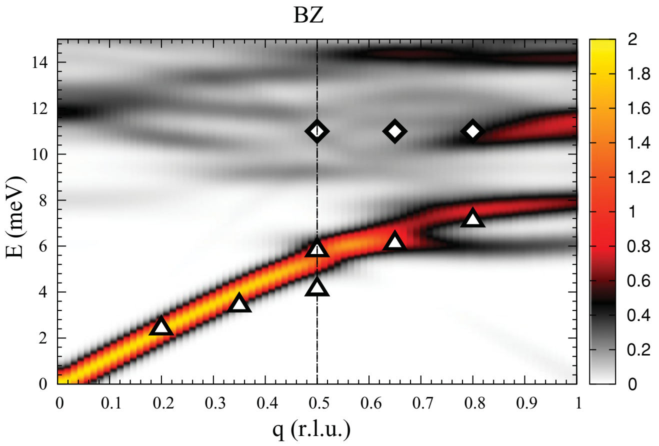

FIG. 9. (Color online) Dispersion relation measured by inelastic x-ray scattering in Mg_2Zn_{11} along the direction $(\xi,4,0)$. Triangles and diamonds stand for acoustic and optical excitations. The dispersion is overlaid on a color coded intensity distribution of the simulated $S(Q,\omega)$ response function. The calculated curves are corrected for a frequency shift $\gamma = 0.2$ following Eq. (10).

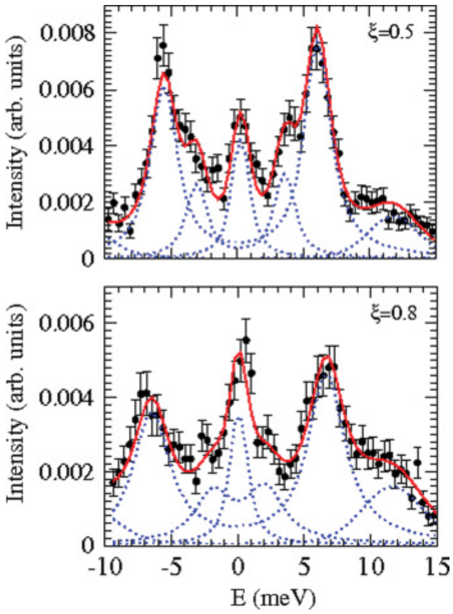

FIG. 10. (Color online) Intensity distribution of the $S(Q,\omega)$ response function measured by inelastic x-ray scattering along (ξ,8,0). The red (solid) curves stand for the fits resulting from the modes depicted as blue (dashed) lines. The gap opening at the zone boundary is nicely visible and marked by an arrow (top panel). The optical excitation at 11 meV is clearly visible in the bottom panel.

of the acoustic excitation, while the normalized intensity is constant for wave vectors inside the Brillouin zone boundary, whereas there is an “intensity transfer” from the acoustic to the optical excitation for larger wave vectors. The bottom panel of Fig. 10 exemplifies the two broad excitations which are observed for larger wave vectors.

We also present the results for measurements carried out along the reciprocal space direction $(4+\xi,\xi,-\xi)$, i.e., for modes propagating along the (1,1,−1) direction. We have investigated this particular direction because simulations predicted it to be close to an instability (see Sec. IV C). Since the (4,0,0) and (1,1,−1) vectors are neither collinear nor orthogonal, both longitudinal and transverse acoustic excitations are measured in this configuration. Indeed both modes are observed as shown in Fig. 11, which displays the dispersion relation, and in Fig. 12, which shows some of the corresponding energy scans. The TA excitation bends over rapidly at an energy of about 4 meV and its intensity vanishes for wave vectors larger than 0.3. The higher-energy longitudinal acoustic excitation also bends over quickly with a maximum energy of 7 meV. Furthermore we find a broad dispersionless optical mode at 12 meV which is, e.g., nicely visible in the bottom left panel of Fig. 12. For further increasing wave vectors the spectrum broadens and is best fitted by two broad excitations with a width of the order of 3.5 meV (FWHM).

In summary these results thus confirm our observations obtained by powder average inelastic neutron scattering. There are very low-lying optical excitations, corresponding to a gap opening for energies of the order of 4.5 meV and with a pseudogap width of about 2 meV. We wish to draw attention to this result, which is rather exceptional for metallic

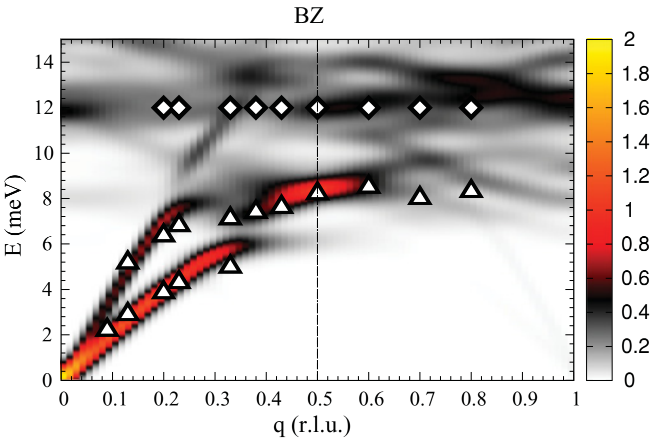

FIG. 11. (Color online) Dispersion relation measured by inelastic x-ray scattering in Mg_2Zn_{11} along the direction $(4+\xi,\xi,-\xi)$ Triangles and diamonds stand for acoustic and optical excitations. The dispersion is overlaid on a color-coded intensity distribution of the simulated $S(Q,\omega)$ response function. The calculated curves are corrected for a frequency shift $\gamma = 0.2$ following Eq. (10).

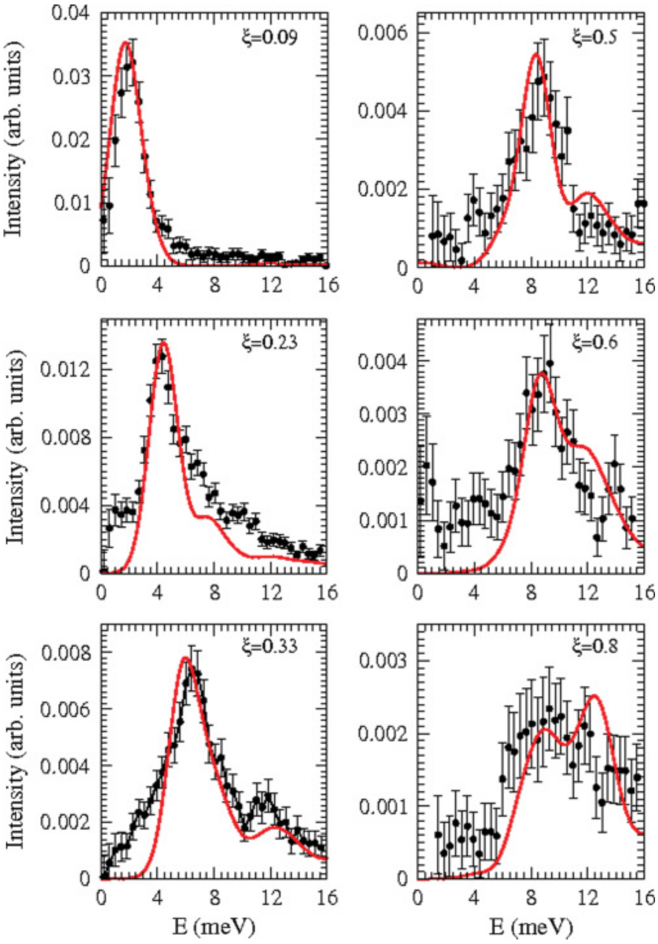

FIG. 12. (Color online) Intensity distribution of the $S(Q,\omega)$ response function measured by inelastic x-ray scattering along $(4+\xi,\xi,-\xi)$. Black dots stand for experimental data, while the red (solid) curves stand for the calculation, corrected for a frequency shift $\gamma = 0.2$ following Eq. (10). The calculated intensities are scaled to fit the experimental data.

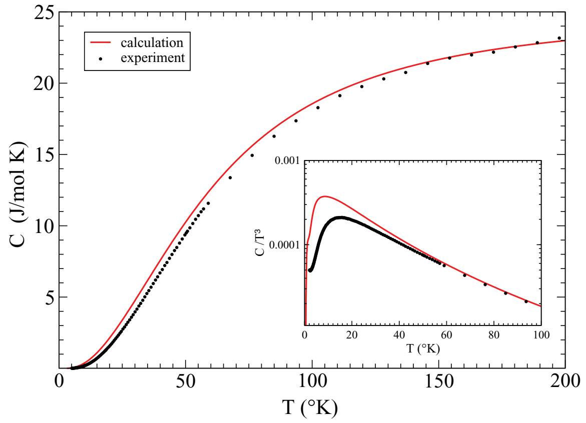

FIG. 13. (Color online) Specific heat in Mg_2Zn_{11}: upper (red) curve, calculation; lower (black) curve, experiment.

alloys. Both the dispersion relation and the measured intensity distribution will be used as strong constraints in comparisons with simulations (see Sec. IV C).

D. Specific heat

To conclude the experimental section we present the results of a specific heat measurement, conducted on a sample of about 30 mm^3 size (Fig. 13). The experimentally determined specific heat is compared to that calculated from the phonon DOS, computed by *ab initio* methods for the $2 \times 1 \times 1$ supercell model with one vacancy as described in Sec. IV B. The differences between experiment and calculation are due to the excess of low-energy modes at 2–3 meV in our calculation, which strongly contributes at low temperatures. On the inset of Fig. 13, C_p/T^3 is depicted to stress these differences. Apart from this the agreement is, however, quite good.

E. Thermal conductivity

The experimentally evidenced low-energy phonon modes in Mg_2Zn_{11} suggest that this material might have a low lattice thermal conductivity κ_l. Indeed, the low-lying optical modes, as well as the acoustic modes, which bend over at energies as low as 4.5 meV and thus lose their dispersive character, are collision channels, which can substantially decrease the lattice thermal conductivity. The anticrossing of the acoustic modes with the low-lying optical excitations, and the resulting reduced average phonon group velocity is known to yield a decrease in κ_l (see for instance Refs. 22–24). Experimentally, the thermal conductivity κ of Mg_2Zn_{11} turned out to be dominated by the electronic contribution κ_e, estimated from the electrical resistivity using the Wiedemann-Franz law. Only in the temperature range from about 10 to 40 K was a significant difference $\kappa_l = \kappa - \kappa_e$ of the order of a few W/mK observed. This is a rather low κ_l value, in good agreement with the experimentally observed GVDOS and dispersion curves of Mg_2Zn_{11}.

IV. COMPUTATIONAL STUDY

The results presented in the following section are obtained from *ab initio* and empirical potential calculations, respectively. The section on energetic stability and the first part of the section on lattice dynamics were calculated using the density functional theory (DFT) code VASP,[25,26] while the second part of the section on lattice dynamics is based on empirical potentials, which have been obtained from *ab initio* data by the force-matching method.[27]

A. Energetic stability

The first part of our energetic study is to confirm the stability of the Mg_2Zn_{11} compound with respect to the competing phases, pure hcp Zn and Laves-phase $MgZn_2$. This is achieved by evaluating the energy difference dE from the tieline connecting Zn and $MgZn_2$ on a composition-energy diagram. The *ab initio* ground state energies of the competing phases have been calculated within VASP, using the projector augmented wave generalized gradient approximation (PAW-GGA) pseudopotential method to account for the core electrons,[28] with medium precision and a carefully converged k-point mesh, adapted to the respective cell geometry. The model of Samson[15] with full occupancy of the Zn1 site is unstable against the tieline by a small, but clear margin of 2.4 meV/atom. On the other hand, if the Zn1 site is left vacant, the total energy lowers and lies only slightly above the tieline. We attempted to find the $T = 0$ K stable superstructure by sampling supercells with up to $2 \times 2 \times 2$ size. Table IX summarizes our results: the optimal superstructure is hexagonal, with three PTR clusters per cell, and 1/3 occupancy of the Zn1 site. We do not claim that this structure is indeed the low-temperature state of Mg_2Zn_{11}. A truly exhaustive study would only be possible with empirical potentials, but so far these have been found to be not accurate enough for such investigations.

The electronic density of states exhibits a pronounced pseudogap, but the fully occupied model shows a spike just at the Fermi level. Optimization of the Zn1 occupancy within supercells clearly affects just these states, as shown in Fig. 14, bringing the pseudogap close to the Fermi level and thus stabilizing the structure.

The occupancy of the Zn1 site definitely affects the vibrational spectrum: mainly, as discussed in Sec. IV B, fully occupied Zn1 sites lead to soft phonon modes, which are close to causing an instability. This is partially cured in supercell models with fractional occupancy of the Zn1 site.

TABLE IX. Energetics of supercell models with fractional average occupancy of the Zn1 site. The first row gives the Pearson symbol, dE is the energy difference in meV/atom from the tieline between pure Zn and the $MgZn_2$ Laves phase, p is the occupancy of the Zn1 site, and a, b, and c are the lattice parameters obtained by relaxation.

		*oP*309	*cP*38	*cF*308	*oC*154	*oP*77	*cP*39
Cell	*hP*117	2×2×2	Unit	2×2×2	$\sqrt{2}\times\sqrt{2}\times1$	2×1×1	Unit
p(Zn1)	1/3	5/8	0/1	4/8	2/4	1/2	1/1
dE	S	0.4	0.4	0.5	0.6	0.8	2.4
a (Å)	11.92	16.92	8.43	16.92	16.92	8.45	8.51
b (Å)	*a*	16.93	*a*	*a*	16.93	8.46	*a*
c (Å)	14.64	16.92	*a*	*a*	8.44	16.88	*a*

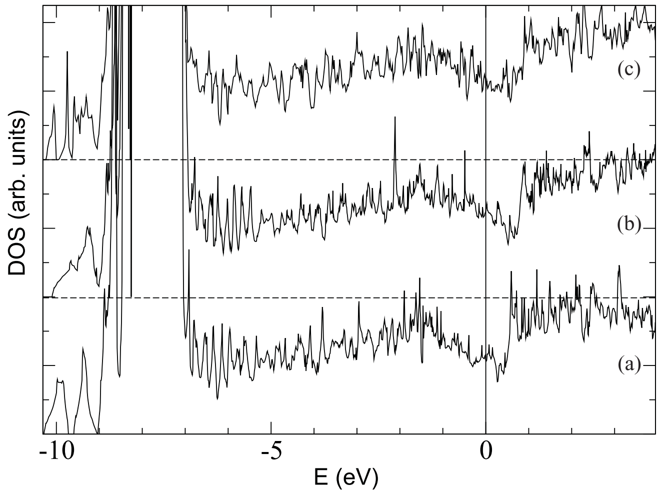

FIG. 14. Electronic density of states of Mg_2Zn_{11} with fully occupied Zn1 site (a), empty Zn1 site (b), and partially occupied (1/3) Zn1 site (c). The solid vertical line shows the Fermi level energy. Models (a) and (b) contain 39 and 38 atoms in the unit cell, respectively. The most stable model (c) has 115 atoms in a triple unit cell, with one out of three Zn1 sites occupied by Zn.

B. Lattice dynamics

1. *Correlation function vs. harmonic approximation*

Lattice dynamics simulations are usually carried out within the harmonic approximation. By inverting the dynamical matrix the dispersion relation (eigenvalues) and the eigenmodes of the phonon states, expressed as Bloch states, are obtained. This also allows calculation of the dynamic scattering function measured in an inelastic neutron (or x-ray) scattering experiment. If it is assumed that lattice vibrations are only small oscillations around the equilibrium position, the interaction between atoms can be described by a force constant model. These force constants are then determined with *ab initio* calculations by applying the Hellmann-Feynman theorem. In the harmonic approximation the dynamic scattering function for up scattering (phonon creation) has the following form:

$$S_{\mathrm{coh}}(Q,\omega) \propto \sum_{j,\vec{Q}_B} F_j(Q)\frac{1}{\omega}[n(\omega,T)+1] \times \delta(\vec{Q}-\vec{Q}_B-\vec{q})\delta(\omega-\omega_j(q)), \qquad (7)$$

$$F_j(Q) = \sum_{\mu}\left|\frac{b^{\mu}_{\mathrm{coh}}}{\sqrt{M_\mu}}\vec{Q}\cdot\vec{e}_{j,\mu}e^{-W_\mu}e^{\vec{Q}\cdot\vec{R}_\mu}\right|^2 \qquad (8)$$

with $\vec{Q}_B$ the Bragg peak position corresponding to elastic scattering, $\vec{q}$ the phonon wave vector, and $F_j(\vec{Q})$ the coherent form factor. The sum runs over all $3N$ vibrational modes. The eigenfrequencies ω and eigenvectors $\vec{e}_i(\omega,q)$ are obtained by inverting the dynamical matrix, which is determined from the *ab initio* force constants. The drawback of this method is that a real system will only comply to a certain extent with a force constant model, which assumes a quadratic interaction potential and thus neglects higher-order terms. Usually this is valid for small displacements of the atoms from their equilibrium positions, meaning that this approximation may become less accurate with increasing temperature.

In the case of anharmonicity, the exact calculation of eigenmodes and eigenvalues is no longer possible within the harmonic approximation. However, as already mentioned in the experimental section, an exact expression of the response function $S(Q,\omega)$ is obtained as the Fourier transform of the density-density correlation function:

$$S(\vec{Q},\omega) = \frac{1}{2\pi N\hbar}\int dt e^{-i\omega t}\sum_{l,m} b_l b_m \langle e^{i\vec{Q}\vec{r}_l(0)}e^{i\vec{Q}\vec{r}_m(t)}\rangle. \qquad (9)$$

The above expression includes all aspects of the dynamics that contribute to $S(Q,\omega)$, i.e., anharmonicities or temperature effects are inherent to this formulation. If this quantity were approached by means of *ab initio* methods, the calculation would be extremely time consuming, even for systems with only a few atoms in the unit cell, not to mention systems having more complex unit cells like CMAs. Therefore this method is better used with effective interaction potentials (see Sec. IV C), avoiding explicit calculation of electronic states.

2. *Ab initio calculations within the harmonic approximation*

Ab initio calculations were conducted with the DFT code VASP,[25,26] again using the PAW method.[28] The unit cell of Mg_2Zn_{11} was relaxed to its electronic ground state with precision set to accurate, since for these kinds of calculation even small errors in the *ab initio* force calculation can yield negative eigenmodes in the vibrational spectrum. For the unit cell calculation the effect of different k-point meshes was studied carefully. From the convergence tests on the Mg_2Zn_{11} unit cell, we concluded that k-point meshes equivalent to a $4 \times 4 \times 4$ mesh in a unit cell calculation (i.e., a $2 \times 4 \times 4$ mesh for a $2 \times 1 \times 1$, etc.) are sufficiently accurate. The relaxation was not terminated before the convergence criterion of residual forces of less than 10^{-4} eV/Å was reached. By subjecting the fully relaxed Mg_2Zn_{11} unit cell to small displacements of one atom at a time (by $\pm$ 0.05 Å), Hellmann-Feynman forces for the resulting, symmetry-nonequivalent configurations were calculated. From these forces, the force constants were extracted and the dynamical matrix was obtained using the PHONON package.[29] After solving the dynamical equations, the response function $S_{\mathrm{coh}}(Q,\omega)$ was computed.

The next step was then calculating $S_{\mathrm{coh}}(Q,\omega)$ using the experimentally accessible (Q,ω) range. To account for the averaging, which is intrinsic in experiments conducted on polycrystalline samples, $S_{\mathrm{coh}}(Q,\omega)$ has to be calculated for a large amount of points in (Q,ω) space. From $S_{\mathrm{coh}}(Q,\omega)$ distributions, obtained in this way, it was now possible to extract the GVDOS, with the same procedure that was used to extract the GVDOS from the experimental data (see Sec. III A). Thus a quantity that is directly comparable to experimental data is obtained.[21] If the accessible Q range is large enough and furthermore the Debye-Waller factor is neglegible (i.e., $e^{-2W} \approx 1$) the GVDOS can also be directly calculated from the PDOS G_μ, as can be seen from Eq. (5). This simplifies the calculation significantly and shows in most cases a good agreement with the calculation. Since the final result depends on the (Q,ω) range, this approximation has, however, to be used with care.

Besides the above-described calculation for Mg_2Zn_{11}, the reference structure $MgZn_2$ was also investigated in detail

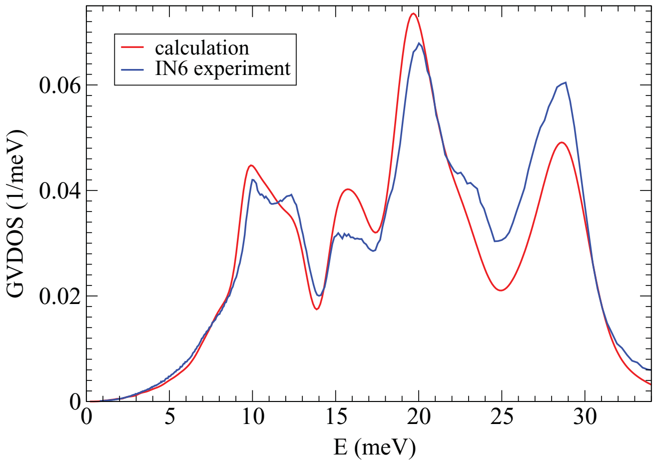

FIG. 15. (Color online) Comparison of experimental [blue (dark gray)] and calculated GVDOS [red (light gray)] for $MgZn_2$ at 300 K. The calculated GVDOS is corrected by frequency shift $\gamma = 0.1$ [see Eq. (10)].

(Fig. 15). The nearly perfect agreement of the calculated and experimentally determined GVDOSs was obtained after introducing a global, constant, relative frequency shift:

$$\omega = (1+\gamma)\omega' \tag{10}$$

where ω' is the calculated eigenfrequency, ω the shifted frequency, and $\gamma = \delta\omega'/\omega'$ the constant relative frequency shift. For $MgZn_2$, we find the optimal $\gamma = 0.1$. After the correction, the maxima observed at 10, 12.5, 15.5, 20, and 29 meV are well reproduced in position and intensity, and even small features like the slight shoulder around 7 meV are clearly visible in our simulation.

The constant-frequency-shift correction has already been applied in $MgZn_2$ single-crystal data analysis[8] and is due to the softening of force constants, an artifact common for the DFT-PAW method.[15,30] Such a correction is also necessary for matching DFT-computed phonon frequency spectra with the experimental GVDOSs of Mg_2Zn_{11}, in which case the optimal $\gamma = 0.07$–0.1.

C. Phonon DOS of Mg_2Zn_{11} by DFT methods

The calculation of phonon eigenstates in Mg_2Zn_{11} requires a supercell approach for two reasons: (i) the unit cube side $a \sim 8.5$ Å may be too small for avoiding spurious finite-size effects on the calculated force constants; (ii) fractional occupancy of the Zn1 site. To disentangle these two effects, we first verified the cell-size impact at full occupancy, comparing the phonon DOS calculated for the unit cell with that of a $2 \times 1 \times 1$ supercell, and found no significant differences. For DFT calculation, we chose the latter supercell as the simplest, most economical representation of the vacancy impact. With an occupation of 50% at the Zn1 site, i.e., with a Zn atom and a vacancy at the cluster center, respectively, we obtain a 77-atom supercell. While this particular choice of vacancy distribution does not minimize the internal energy (see Table IX), the shape and symmetry of the supercell grant good k-point convergence and efficiency of the DFT calculation.

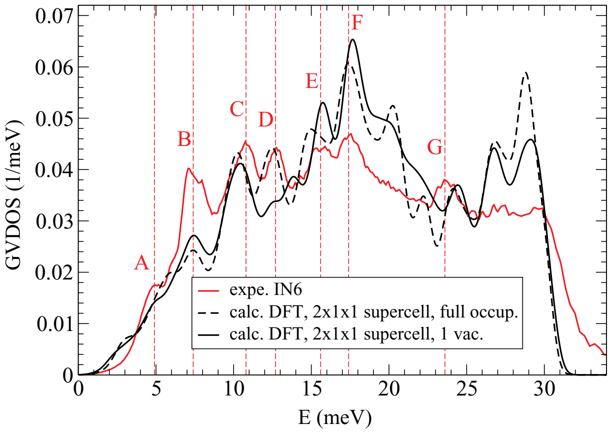

FIG. 16. (Color online) Comparison of experimental and calculated GVDOSs for Mg_2Zn_{11}, for double-supercell models with full or half occupancy of the Zn1 site. A uniform frequency shift of $\gamma = 0.07$ [see Eq. (10)] is applied. Peaks on the IN6 GVDOS are labeled following Table VII.

Figure 16 shows the GVDOSs for the two models (full occupancy, one vacancy), along with the experimental GVDOS determined on the IN6 spectrometer at room temperature. The comparisons are facilitated by the peak labeling scheme from Table VII . To better match experiment and calculation a uniform frequency shift of $\gamma = 0.07$ has been applied, following Eq. (10).

Generally, both models show very good correspondence with the experimental data. Practically all maxima A through G found for the experimental DOS have their counterpart in the calculated DOSs. The high-energy part of the spectrum appears overestimated in the calculation, but in fact the temperature-dependent, experimental study on the IN4 spectrometer clearly shows an increase of the DOS exactly in the region $E > 25$ meV (see Fig. 7), as the temperature is decreased from 300 to 100 K. The only apparent discrepancies are seen in the low-energy part, showing significant excess of states in the calculation. Although the group of extremely low-lying opticlike modes around 3 meV, which is responsible for this excess, is affected by the choice of the particular vacancy distribution, it never disappears. After verifying that these modes persist in all our k-point convergence tests (for unit cell k mesh set to $6 \times 6 \times 6$) and supercell variations [in addition to the double supercell mentioned above, we studied a $2 \times 2 \times 2$ face-centered supercell, as well as a $(0.5,0.5,0) \times (0.5,0,0.5) \times (1,0,0)$ supercell], the unit cells with and without vacancy were also calculated by linear response theory (LRT) to make sure that these modes are not due to the finite-displacement method. Since the LRT calculation also evidenced the same problem, we have to consider the occurence of these modes as an unavoidable artifact of our DFT calculation. By comparing the results obtained for the fully and partially occupied $2 \times 1 \times 1$ supercell we find that a vacancy at one of the Zn1 sites slightly increases the height of maximum B, increases the DOS between 21 and 24 meV, and decreases the high-energy ($E > 25$ meV) maximum (the last effect is similar to the experimentally observed T-dependent intensity damping). However, the most pronounced effect is visible for maximum D: the full-occupancy model evidences a strong maximum at slightly lower energy than the experiment, while the maximum is split into two submaxima for the model with one vacancy, the smaller one being exactly at the energy of D, the second one about 1 meV above. Interestingly, the maximum D shows a clear T-dependent energy shift in the IN4 experiment (Fig. 7), and in Sec. IV E we demonstrate that this mode is mainly due to vibrations of the Zn5 icosahedron, which is naturally most affected by the presence of a vacancy at its center.

To conclude, practically all phonon DOS variation caused by the presence of vacancies is compatible with the experimentally observed GVDOS. The maximum that is crucially affected by the vacancies is D. We think the fact that our double-cell model does not accurately account for the energy and height of this maximum is due to the fact that other vacancy distributions are energetically more favorable. The limitations of DFT methods do not allow us to study this effect in a more systematic way and therefore the next section is devoted to the study of this phenomenon using an adapted Hamiltonian and embedded atom method (EAM)–potentials.

1. Impact of vacancy distribution on lattice dynamics: A study based on effective potentials

As addressed in the last section, DFT imposes strong limits on the feasible system size, making in our case only a few, distinct vacancy distributions accessible for *ab initio* methods. A way to overcome this deficiency is the use of effective potentials. In this section, we present a detailed study of the influence that certain vacancy distributions exert on the dynamics of Mg_2Zn_{11} by means of molecular dynamics (MD) using EAM potentials. The EAM potentials that have been used for our purpose have been fitted to *ab initio* data[31,32] by the force matching method,[27] using the code POTFIT.[31]

For a $2 \times 2 \times 2$ supercell, containing eight Zn1 sites, we considered *all possible* distributions of one to eight vacancies, and calculated the dynamic structure factors (still within the harmonic approximation). From comparison with the experimental dispersion curves (Figs. 9 and 11), we found the best agreement for a model with a vacancy content of 50% (i.e., 308 atoms with four Zn and four vacancies at the Zn1 site) and a highly symmetric arrangement of these vacancies. This arrangement is equivalent to a structure with space group $Fm\overline{3}$ and eight Wyckoff sites (seven Zn sites and one Mg site). For a more constraining test we then compared our simulations to the experimental $S_{\mathrm{coh}}(Q,\omega)$ intensity distribution, measured on single-grain samples by inelastic x-ray scattering (Fig. 12). The influence the vacancy content has on the dynamical properties of the structure becomes evident when the dispersion curves along the (111) direction for the unit cell and $2 \times 2 \times 2$ supercell with 50% vacancy at the cluster center are compared, as shown in Fig. 17. The calculation for the fully occupied unit cell displays two almost unstable acoustic branches bending over at low q and very low energy: the acoustic range is thus extremely limited (up to 2 meV for TA and 3 meV for LA modes), which is consistent with this model being less stable, as discussed previously. Such a low-energy bending of the acoustic mode is not what is observed experimentally (see Figs. 9 and 11). The situation is dramatically changed in the supercell model where now the transverse and longitudinal regimes are well defined with a linear dispersion up to 4 and 6 meV, in good agreement with the experiment. Due to the increased atom number further optical branches emerge in the supercell model—in both cases the number of phonon branches is $3N$, meaning that in the unit cell we find 3×39 branches while the supercell model evidences 3×308.

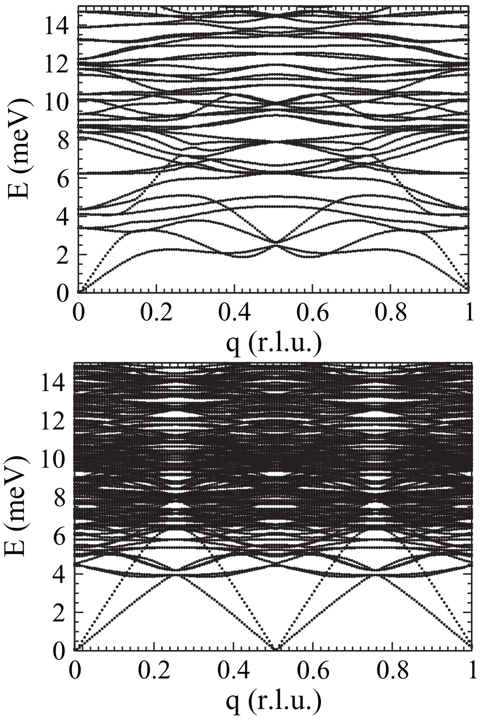

FIG. 17. Simulated dispersion curve along the direction $(4+\xi,\xi,-\xi)$ using EAM potentials (see text). Top: Fully occupied unit cell. Bottom: $2 \times 2 \times 2$ supercell with 50% vacancies.

The crucial point is now that these additional modes occur above 5 meV and that many of them are almost degenerate or evidence a vanishing dynamic structure factor, resulting in the $S_{\mathrm{coh}}(Q,\omega)$ distribution depicted in Fig. 9. Thus the introduction of the Zn-vacancy disorder is translated into a distribution of broad modes in $S_{\mathrm{coh}}(Q,\omega)$, still presenting clear maxima. This is consistent with the general statement that disorder introduces a broadening of the optical excitation and is in good agreement with the observed broad maxima at high energy in $S_{\mathrm{coh}}(Q,\omega)$.

One prominent feature of the experimental data is the occurrence of a gap in the dispersion relation of the TA modes measured around the (0,4,0) Bragg reflection and propagating along (1,0,0). A comparison between experimental dispersion and simulation is presented in Fig. 9, where the weakly convoluted simulated $S_{\mathrm{coh}}(Q,\omega)$ response function is superimposed on the experimental dispersion relations, shown as triangles and squares. After applying a uniform frequency shift of $\gamma = 0.2$ [following Eq. (10)] we obtain a good overall agreement between dispersion relation and simulation. However, a significant difference is observed close to the zone boundary, where the TA mode evidences a gap of about 2 meV, which is much larger than the one obtained from the simulation conducted for our model. This discrepancy is to be related to still existing differences at low energy in the GVDOSs. At this point it has to be noticed that the comparison is much improved as compared to simulations carried out without vacancies, pointing out again the importance of having included such disorder. The comparison for modes propagating along the (1,1,−1) direction (see Fig. 11) is also quite good. The two LA and TA modes are well reproduced by the frequency-corrected simulation (again a uniform frequency shift of $\gamma = 0.2$ is applied) and a pseudogap between the two branches at 4.5 and 6.5 meV is well visible. Again the results are much improved as compared to simulations without vacancies, in which an almost unstable low-energy mode was calculated for this direction in reciprocal space. Besides the overall agreement of the dispersion relation, we also obtained a semiquantitative agreement when comparing the experimental intensity distribution of the $S_{coh}(Q,\omega)$ response function to that one calculated for our model (Fig. 12). For this comparsion the simulated structure factors are convoluted by a Gaussian of width 2 meV (FWHM), which is approximately equivalent to the instrumental resolution. The agreement between experimental data and the calculated, frequency-corrected structure factors for the $2 \times 2 \times 2$ supercell model is quite good—the acoustic modes and their intensity ratios are well reproduced and also the broad maxima of optical modes, resulting from the Zn vacancy disorder, fit the experimental results. Here, one has to keep in mind that the $S_{coh}(Q,\omega)$ intensity distribution is a very constraining test, since $S_{coh}(Q,\omega)$ is directly related to the eigenvectors of the different phonon modes [see Eq. (8)].[5,33]

2. *Influence of temperature on lattice dynamics studied by molecular dynamics with effective potentials*

Finally, we have investigated the effect of temperature on the GVDOS of Mg_2Zn_{11}. Similarly to other experiments,[34,35] raising the temperature induces a smearing of the measured GVDOS, especially at high energies (Fig. 7). This effect can be rather well reproduced when MD simulations are used to obtain the GVDOS. Indeed, by computing the Fourier transform of the time-dependent velocity-velocity autocorrelation function, the GVDOS can be calculated from MD particle trajectories. For this purpose, the MD trajectories of the aforementioned supercell model [$2 \times 2 \times 2$ supercell with 4 out of 8 Zn1 positions being vacant] were extracted from MD runs conducted with the IMD package for different temperatures,[36] also using EAM potentials. With these trajectories the GVDOS was then calculated by use of the software package NMOLDYN.[37]

Our simulations produce a GVDOS smearing with rising temperature, similar to that in the experiment, which can be roughly accounted for by a Gaussian smearing whose width is proportional to the energy. In addition we observe a strong damping of the high-energy peaks (see Fig. 18), when the IN4 experimental and the simulated GVDOSs are compared at 300 and at 100 K, respectively. The temperature-dependent damping effect explains why strong peaks present in the harmonic calculation (Fig. 16) are not seen in room temperature experiments (while they are present in the $T = 100$ K IN4 GVDOS in Fig. 7). Whereas peak *B* is almost perfectly reproduced for the 100 K case it is hardly visible for the MD calculation conducted at 300 K. This behavior, the strong change of peak *D* with temperature, as well as the differences between the low-temperature MD calculation and *ab initio* calculations for smaller supercells, indicate that the EAM potential is not able to perfectly reproduce the GVDOS of Mg_2Zn_{11}. However, the tendency of decreasing intensity for phonon modes above ∼15 meV with an increase in temperature is clearly visible, thus explaining parts of the differences between *ab initio* calculations and experimental data.

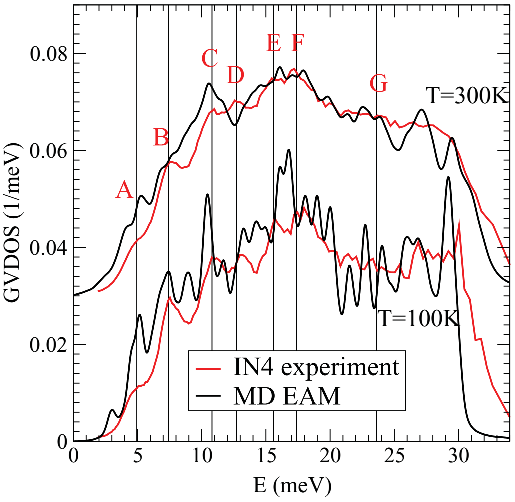

FIG. 18. (Color online) Comparison of the experimental GVDOS [red (light gray)] and the GVDOS calculated with MD for the $2 \times 2 \times 2$ supercell with 50% vacancy at the cluster center (black) at 100 and at 300 K. $\gamma = 0.1$ [see Eq. (10)]; peak labels as in Table VII.

D. Partial density of states

In this section, we analyze in detail the DFT calculation of the lattice dynamics in our double-supercell model with the Zn1 site being occupied by one Zn atom and one vacancy. The total phonon DOS of this model was in good agreement with the experimental results as was already discussed in Sec. IV C.

The phonon DOS projected on the Wyckoff sites ("partial" phonon DOS; Fig. 19) reveals the unusual character of the vibrational modes in Mg_2Zn_{11}: the partial DOS of each Wyckoff site has its own distinct character. This feature was already evident from the presence of many maxima in the experimental GVDOS, which is in contrast to the lattice dynamics of aluminum-based complex structure alloys like $Al_{13}Co_4$, whose GVDOS is almost featureless.[34,35]

First, the Mg partial DOS in Fig. 19 reveals a small contribution of Mg in vibrations with $E < 15$ meV, and a double peak at 27 and 30 meV which is evident in the 100 K IN4 GVDOS (see Fig. 7).

Most importantly, for practically all GVDOS maxima labeled in the figure, the partial DOS reveals the characteristic site contributions: the Zn2 octahedron, Zn3 ("large" icosahedron), and Zn4 dodecahedron are responsible for the very-low-energy maxima *A* and *B*; while the Zn5 icosahedron together with the Zn4 dodecahedron contribute prominently at *C* and *D*. The maximum *E* is due to Mg and the Zn5 icosahedron, while the maximum *F* is like *E*, with an additional strong contribution of the Zn2 octahedron. Finally, peak *G* is dominated by the Zn5 icosahedron.

Overall, it is surprising to see that the Zn2 octahedron has a strong participation in the lowest-energy vibrations, and then

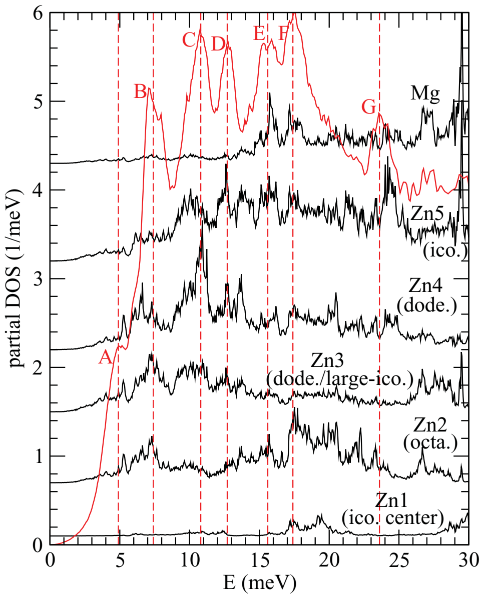

.

FIG. 19. (Color online) Partial densities of states for the Mg_2Zn_{11} Wyckoff sites ($2 \times 1 \times 1$ supercell with one vacancy at Zn1) (black curves). GVDOS obtained from the IN6 instrument [red (light gray) curve]. Peak labels are as in Table VII. The partial DOSs are weighted by site multiplicities.

again at rather high energies (maximum F). The outer shells of the clusters (Zn3 and Zn4) are the "loose" part of the structure, with dominant contributions at low energies (maxima A–C). The Zn5 icosahedron is absent in the lowest-energy maxima A and B, but then significantly participates at practically all prominent vibrations at higher energies. In the following section, we offer a graphical interpretation of the atomic motions constituting the vibrational modes.

E. Mode analysis

While the two- or even three-shell cluster description introduced in Sec. II C reveals structural relationships, it is not quite relevant for analyzing vibrational modes, due to the weak metallic bonding, but also due to the relatively small size of the cubic unit cell, leading to strong cubic distortions of the outer, topologically icosahedral cluster shells. For the purpose of efficient graphical representation of phonon eigenmodes, we find another, layer-based description of the structure more suitable. We notice that four well-defined layers form along the twofold (c, for example) direction: a flat layer F_{cub} at $z = 0$, a puckered layer P for $0.163 \leqslant z \leqslant 0.343$, F_{ico} at $z = 0.5$, and an inverse puckered layer P'. Since the puckered layers are equivalent by symmetry, the entire structure may be represented by a sequence of the three layers F_{cub}, P, and F_{ico}. We call the first flat layer "cubic" because it is dominated by a proper fcc local cluster, composed of a Zn2 octahedron and Zn4 cube (outlined in Fig. 22, bottom, left panel); even a further shell of Zn3 atoms are close to fcc positions. The second flat layer is denoted "icosahedral' as it contains the Zn5 icosahedron (extending into P layers, outlined in the bottom right panel of Fig. 22). A useful diagnostics of phonon eigenmodes is the participation ratio (PR),[38] defined as

$$p_j(\omega) = \left(\sum_{\mu=1}^{3N} \frac{|\vec{e}_{j,\vec{q},\mu}|^2}{m_\mu}\right)^2 \Bigg/ N \sum_{\mu=1}^{3N} \frac{|\vec{e}_{j\vec{q},\mu}|^4}{m_\mu^2}. \qquad (11)$$

When the PR→1 all atom displacements are (almost) equal for the atoms of a species; such eigenstates are collective excitations. When the PR→ 0 only a few atoms have large displacements; such eigenstates are localized excitations.

In metallic alloys with complex structure, we may expect interesting interactions between propagating collective excitations, and either opticlike modes with unusually low frequencies, or anomalously loose atoms supporting localized, potentially anharmonic vibrations. Figure 20 shows the PR of the double-supercell model, discussed in the previous section, with one Zn and one vacancy on the Zn1 site. The bottom panel shows the calculated DOS and the experimental GVDOS for reference. The instability (artifact of our DFT calculation) is clearly visible as a cloud of points around 2–3 meV with low PR ~ 0.4. The clear difference between the groups of modes belonging to A and B is that the former spans a large PR interval from 0.2 to 0.7, while the latter evidences a PR ~ 0.5. The high-energy vibrations are dominated by light Mg atoms, so not surprisingly these modes have a tendency to localize. More noticeably, *every* maximum in the DOS is accompanied by an abrupt decrease of the PR. This phenomenon is most pronounced for peaks F, and especially E.

Finally, we turn to the graphical visualization of the phonon eigenmodes. Due to the structural complexity, it is not practical to study individual eigenmodes. Apparently, the groups of modes that have nearly equal energy and PR are closely related. In Figs. 21 and 22 we use the layer-decomposition

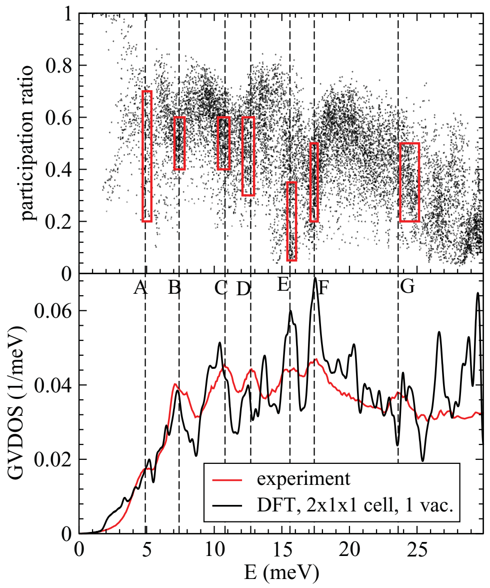

FIG. 20. (Color online) Participation ratio and density of states of Mg_2Zn_{11}, both after uniform frequency shift correction $\gamma = 0.07$ [see Eq. (10)]. Eigenmodes with frequency and participation from the A–G windows, shown as red rectangles in the upper panel, are selected for graphical representation in Figs. 21 and 22.

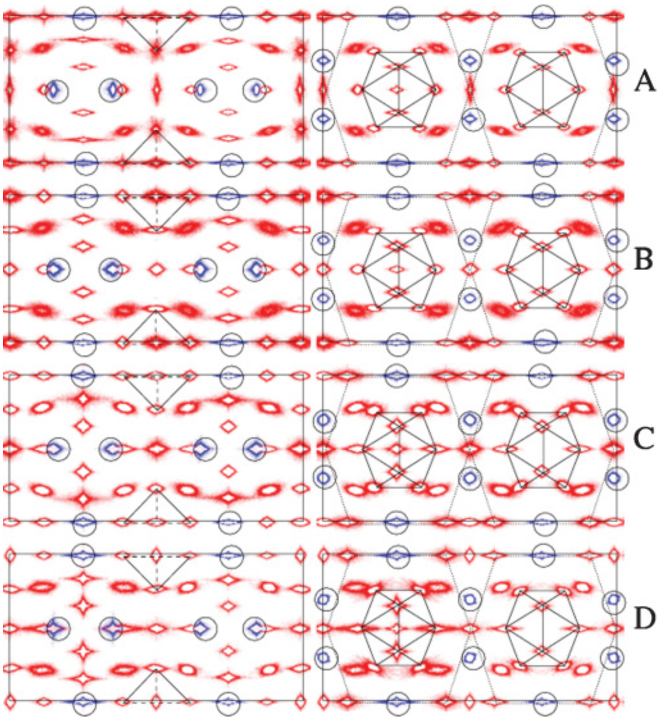

FIG. 21. (Color online) Time-averaged particle density plots for slabs projected along the twofold axis of Mg_2Zn_{11}. Spatial particle motions are due to time evolution of vibrational eigenstates obtained from the DFT dynamical matrix (for a $2 \times 1 \times 1$ supercell with two Zn1 sites containing one Zn and one vacancy). The selected range of eigenmodes, represented in windows A–D, corresponds to the marked rectangular areas in the energy-participation plot (Fig. 20). The Mg atom density is shown in blue-scale (gray and marked by a circle) for densities up to 5% of maximal density, otherwise white; for Zn the same is valid in red-scale (gray, without circle). The left column panels contain the "cubic" flat layer at $z = 0$, together with the puckered layer $0.163 \leqslant z \leqslant 0.343$. The right column panels contain the same puckered layer, and the "icosahedral" flat layer at $z = 0.5$ (so the puckered layer is shown in both columns).

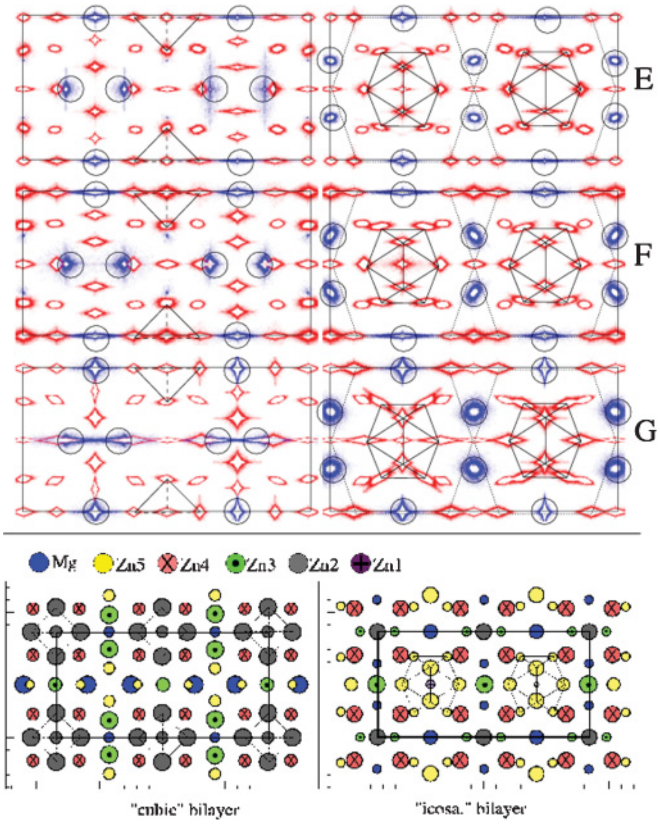

FIG. 22. (Color online) Time-averaged density as in Fig. 21, but for windows E–G. The bottom panel is a plot of the atomic structure along the same axis, and using the same layers. Size of the circles is proportional to the height z of an atom. Wyckoff sites are shown in different colors (different gray scale plus marks).

described above to depict selected groups of related modes, for the DOS maxima A–G. For each group, the selection "window" is outlined by the rectangular boxes in the upper panel of Fig. 20. To visualize the motion of each atom, we divide each eigenmode into 100 time frames and interpolate its time evolution. From the time evolution of each eigenmode the accumulated atomic density (i.e., the probability to find an atom at a certain position) is extracted and projected down along the twofold axis. Zn atoms are shown as red–scale (gray–scale), Mg atoms as blue–scale (gray–scale, marked by a circle), for densities up to 5% of the maximal density. The 5% –100% range is displayed simply as white—this area, near the equilibrium position, has a steeply increasing intensity.

The left panels in both figures show a union of the layers $F_{\mathrm{cub}}+P$, whereas the right panels show $P+F_{\mathrm{ico}}$. In the left column, Zn2 octahedra and in the right column Zn5 icosahedra are outlined. The bottom-most panels in Fig. 22 show the atomic structure of the respective bilayers, using color codes for Wyckoff sites with circle sizes being proportional to the z coordinate. Notice that in the right column of the panels, which contains the F_{ico} layer, the left icosahedron is filled by Zn1, whereas the second icosahedron on the right is *vacant*.

The first obvious impression is that Fig. 21 is dominated by vibrations of the heavier Zn atoms (red, gray), while Fig. 22 seems to be rather dominated by light Mg (blue, circled) atoms. As mentioned in Sec. IV D, the lowest-energy groups at maxima A and B are Zn2, Zn3, and Zn4 atoms. The difference between A and B is mainly that A is more anisotropic, for Zn3 atoms in particular. For group C and D, the Zn5 icosahedron becomes active.

Although Mg atoms are light atoms and thus have vibration energies localized at higher energies, they also display motions at low energies, as is visible in panels A, B, C, and D. Strong motions of the Mg atoms are, however, found for panels E, F, and G, which cover the frequency range that also showed high contributions of the Mg partial DOS. Especially the anisotropic motions depicted in panel E can directly be related to the cigar -shaped ADPs which have been found experimentally. Indeed, by calculating the ADPs from the obtained phonon eigenmodes, it can be shown that modes in the frequency range of peak E strongly contribute to the ADPs of Mg. From what was discussed in Sec. II B it is clear that the loose atomic environment of the Mg atoms gives rise to their anisotropic motion inside the elongated Zn cages.

The most interesting phenomenon is associated with the group of modes at maximum D: evidently this is the only case showing strong impact of doubling the cell, and atom-vacancy alternation at the Zn1 site. This can be seen as intensity variation for both bilayers, when looking at the left (right) parts of the figures, as the modes at the filled icosahedron show stronger localization (and larger displacement amplitude). The same is true for the Zn4 atoms, which form the second, dodecahedral shell around the Zn5 icosahedron. By regarding the phonon DOS (bottom panel of Fig. 20), we can see that the calculated *D* maximum is actually split into two peaks, as discussed in Sec. IV C. Although the upper submaximum at about 14 meV does not match any experimental feature, the full-occupancy model also fails by overestimating maximum *D*. We suspect that the appropriate distribution of vacancies would give a better match for the experimentally observed maximum.

We also point out that peak *D* has been found to show an appreciable shift in temperature 100–300 K (IN4 experiment; see Sec. III B). We therefore believe that this particular peak is a sensitive (indirect) probe of the vacancy distribution on Zn1 site.

The modes in Fig. 22 show two distinct vibrational scenarios. The modes at maxima *E* and *F* are essentially vibrations of the Zn5 icosahedra plus Mg atoms. Clearly, it is mainly the Mg atoms that are responsible for the dramatic localization tendency (especially at maximum *E*). In contrast to this, the modes at *G* are vibrations that are driven by the Zn5 icosahedron only. While this is clearly a "cluster" vibrational mode, it apparently strongly breaks icosahedral symmetry. However, seeing such clear evidence of well-defined cluster vibrations, we look forward to the analysis of eigenmodes in "more icosahedral" structures like τ-AlMgZn, which is built from large three-shell icosahedral clusters.

V. SUMMARY AND DISCUSSION

We have performed a combined experimental and computational study of the Mg_2Zn_{11} phase, structurally related to the Bergman (τ-AlMgZn) and Laves phases ($MgZn_2$) on one hand, but also to the $ScZn_6$ structure, built from so-called Tsai clusters.

The atomic structure of Mg_2Zn_{11} has been refined using data from x-ray and neutron scattering experiments, revealing the previously unnoticed partial occupancy of the Zn1 site, along with the strongly anisotropic ADPs for some atomic sites, most notably for the Mg atoms. Such vibrational motion is a consequence of the low-symmetry Mg coordination shell with 17 neighboring atoms, violating the Frank-Kasper tetrahedral space-filling rule.

The previously unnoticed feature of partial occupancy at the icosahedrally coordinated Zn1 site has important impact on the energetic stability of the Mg_2Zn_{11} phase. From our DFT calculations (Sec. IV A) it is evident that the fractional occupancy of Zn1 is a genuine low-temperature feature: various superstructures with distinct atom and vacancy distributions on the Zn1 site lower the total energy with respect to the tieline between models with only Zn or only vacancies at the Zn1 site. Finding the true low-temperature state of Mg_2Zn_{11}, however, exceeds the feasibility of *ab initio* methods, and we have left this task for future investigations.

The dynamical properties were probed by neutron inelastic scattering on two different instruments, including a temperature-dependent setup. The neutron experiments revealed a vibrational DOS, exhibiting surprisingly many sharp, well-defined features, indicating that despite structural complexity, several families of eigenmodes retain their distinct character. Furthermore, a first singularity is found at an energy of about 4.5 meV, which is a rather exceptional feature for a close-packed metallic alloy as can be seen from comparison with $MgZn_2$, $ScZn_6$, or even pure Zn. In the GVDOS of $MgZn_2$ we find a small bump at $\sim$7 meV (see Fig. 5), which is due to the lowest-energy acoustic branch,[9] the dispersion curves of $ScZn_6$ show a gap opening at about 8 meV,[5] and in pure Zn a soft TA mode, propagating along [100] and related to the c/a ratio, is found at roughly 6.5 meV.[11] None of these structures, however, evidences singularities at such low energies as does Mg_2Zn_{11}. The study of the temperature dependence showed that anharmonic effects in the low-energy part of the Mg_2Zn_{11} spectrum can be neglected (peaks at 4.5 and 7 meV, respectively), whereas the energy of the peak at $\sim$13 meV clearly decreased with increasing temperature. In the high-energy part of the GVDOS around 30 meV, low-temperature (100 K) data showed much higher density of states than the room temperature data.

Finally, phonons corresponding to the anomalously low-energy maxima in the GVDOS around 4.5 and 7 meV were directly probed by inelastic x-ray scattering experiments for a small Mg_2Zn_{11} single crystal. A clear gap opening (width $\sim$2 meV) resulting from an interaction of acoustic and optic modes was observed, in agreement with the results obtained from inelastic neutron scattering.

In our computational approach, phonon spectra were calculated in the harmonic approximation by diagonalizing the dynamical matrix, or by evaluating the velocity autocorrelations from molecular dynamics simulations, using either the *ab initio* DFT method or fitted empirical EAM potentials. We first clarified that models with fully occupied Zn1 sites were prone to phonon instabilities. Optimal comparison with experimental data was achieved for supercell models in which Zn atoms filled only subsets of the Zn1 sites. However, fine agreement between experimental and calculated GVDOSs was only achieved after applying a constant, relative shift to the calculated eigenfrequencies, indicating systematic softening of the force constants calculated by the DFT method.

Due to the feasibility limitations of the DFT method for supercells containing hundreds of atoms, our study of temperature dependence was conducted with molecular dynamics in a $2 \times 2 \times 2$ supercell using empirical EAM potentials. These simulations showed similar trends as were found experimentally, like the increase of modes at high energies for low temperatures or the smoothing of the whole spectrum when the temperature is increased. The systems we have investigated are model systems; however, due to the good agreement between various experimental results and calculations, it is justified to use them to interpret the dynamics on an atomistic level.

In materials with such a complex structure, vibrational modes cannot be meaningfully analyzed one by one. In order to achieve a systematic microscopic interpretation, in Secs. IV D and IV E we diagnosed modes, using their participation ratio as a quantity indicative of the degree of their mutual similarity. Groups of modes with similar energy *and* participation ratio were then analyzed graphically by constructing time-averaged distributions, which illustrate characteristic atomic motions. We could clearly demonstrate that the prominent modes with anomalously low energy at 5 and 7 meV (labeled *A* and *B*, respectively) correspond to atomic motions of Zn2, Zn3, and Zn4 atoms, while the mode *D* at 13 meV can be attributed to vibrations of the Zn5 atoms of the icosahedron. From a structural point of view this is closely related to the nonideal coordination shells we found for these atoms, giving them more space as in a perfectly close-packed structure.

We expect that even more complex structures with larger unit cells can be analyzed in a similar manner. Although Mg_2Zn_{11} consists of remarkably large (overlapping) clusters, we suspect that the unit cell is too small for characteristic "cluster modes" to develop; in this respect we look forward to studying larger, even more complex structures like Bergman-phase AlMgZn.

Finally, it should be pointed out that the special low-energy modes *A* and *B* are *not* generic to the structure, but rather a consequence of the anomalous Zn-Zn interaction: our DFT calculations for the isostructural ternary compound $Mg_2Cu_6Al_5$ show no trace of such excitations.

ACKNOWLEDGMENTS

We wish to thank M. Widom for providing the linear response calculation in Sec. IV C. The support from the European Comission Network of Excellence on Complex Metallic alloys (Grant No. NMP3-CT-2005-500140) is gratefully acknowledged. M.M. also acknowledges partial support from VEGA Grant No. 2/0157/08. Furthermore we gratefully acknowledge the allocation of beam time by ILL and ESRF.

---

[*] euchner@itap.physik.uni-stuttgart.de

[1] C. Janot, *Quasicrystals: A Primer* (Clarendon Press, Oxford, 1994).

[2] T. Janssen, G. Chapuis, and M. de Boissieu, *Aperiodic Crystals*, IUCr Monographs on Crystallography, Vol. 20 (Oxford Science Publications, Oxford, 2007).

[3] A. P. Tsai, J. Q. Guo, E. Abe, H. Takakura, and T. J. Sato, Nature (London) **408**, 537 (2000).

[4] C. P. Gomez and S. Lidin, Phys. Rev. B **68**, 024203 (2003).

[5] M. de Boissieu, S. Francoual, M. Mihalkovic, K. Shibata, A. Q. R. Baron, Y. Sidis, T. Ishimasa, D. Wu, T. Lograsso, L. Regnault, F. Gähler, S. Tsutsui, B. Hennion, P. Bastie, T. J. Sato, H. Takakura, R. Currat, and A. P. Tsai, Nat. Mater. **6**, 977 (2007).

[6] M. de Boissieu, S. Francoual, R. Currat, and E. Kats, Phys. Rev. B **69**, 054205 (2004).

[7] G. Bergman, J. L. T. Waugh, and L. Pauling, Acta Crystallogr. **10**, 254 (1957).

[8] P. Brommer, M. de Boissieu, H. Euchner, S. Francoual, F. Gähler, M. Johnson, K. Parlinski, and K. Schmalzl, Z. Kristallogr. **224**, 97 (2009).

[9] S. Francoual, M. de Boissieu, R. Currat, K. Shibata, Y. Sidis, B. Hennion, and A. P. Tsai, J. Non-Cryst. Solids **353**, 3182 (2007).

[10] D. L. McDonald, M. M. Elcombe, and A. W. Pryor, J. Phys. C **2**, 1857 (1969).

[11] L. Almqvist and R. Stedman, J. Phys. F **1**, 785 (1971).

[12] D. Singh and D. A. Papaconstantopoulos, Phys. Rev. B **42**, 8885 (1990).

[13] T. Ishimasa, Y. Kasano, A. Tachibana, S. Kashimoto, and K. Osaka, Philos. Mag. A **87**, 2887 (2007).

[14] H. Takakura, C. P. Gomez, A. Yamamoto, M. de Boissieu, and A. P. Tsai, Nat. Mater. **6**, 58 (2007).

[15] S. Samson, Acta Chem. Scand. **3**, 835 (1949).

[16] V. Petříček, M. Dusek, and L. Palatinus, computer code JANA2006 [http://jana.fzu.cz/].

[17] J. D.Corbett and Q. S. Lin, Inorg. Chem. **43**, 1912 (2004).

[18] Q. S. Lin and J. D. Corbett, Philos. Mag. A **81**, 777 (2001).

[19] G. L. Squires, *Introduction to the Theory of Thermal Neutron Scattering* (Cambridge University Press, Cambridge, 1978).

[20] H. Zabel, in *Neutron and Synchroton Radiation for Condensed Matter Studies*, (edited by J. Baruchel) (1993), Vol. I, pp. 286–320.

[21] H. Mutka, M. R. Johnson, M. M. Koza, and L. Capogna, Nucl. Instrum. Methods **600**, 226 (2009).

[22] J. S. Tse, V. P. Shpakov, V. R. Belosludov, F. Trouw, Y. P. Handa, and W. Press, Europhys. Lett. **54**, 354 (2001).

[23] T. Takeuchi, N. Nagasako, R. Asahi, and U. Mizutani, Phys. Rev. B **74**, 054206 (2006).

[24] M. Christensen, A. B. Abrahamsen, N. B. Christensen, F. Juranyi, N. H. Andersen, K. Lefmann, J. Andreasson, C. R. H. Bahl, and B. B. Iversen, Nat. Mater. **7**, 811 (2008).

[25] G. Kresse and J. Hafner, Phys. Rev. B **47**, 558 (1993).

[26] G. Kresse and J. Furthmüller, Phys. Rev. B **54**, 11169 (1996).

[27] F. Ercolessi and J. B. Adams, Europhys. Lett. **26**, 583 (1994).

[28] G. Kresse and D. Joubert, Phys. Rev. B **59**, 1758 (1999).

[29] K. Parlinski, COMPUTER CODE PHONON, version 4.28, 2005 [http://wolf.ifj.edu.pl/phonon/Public/phrefer.html].

[30] K. Parlinski (private communication).

[31] P. Brommer and F. Gähler, Modell. Simul. Mater. Sci. Eng. **15**, 295 (2007).

[32] P. Brommer, Ph.D. thesis, Universität Stuttgart, 2008.

[33] N. J. Chesser and J. D. Axe, Phys. Rev. B **9**, 4060 (1974).

[34] J. Suck and M. Scheffer, J. Non-Cryst. Solids **334-335**, 295 (2004).

[35] *Quasicrystals—An Introduction to Structure, Physical Properties, and Applications*, edited by J.-B. Suck, M. Schreiber, and P. Haussler, Materials Science, Vol. 55 (Springer, Berlin, 2002).

[36] J. Stadler, R. Mikulla, and H.-R. Trebin, Int. J. Mod. Phys. C **8**, 1131 (1997).

[37] T. Róg, K. Murzyn, K. Hinsen, and G. R. Kneller, J. Comput. Chem. **24**, 657 (2003) [http://dirac.cnrs-orleans.fr/nMOLDYN/index.html].

[38] M. Krajči and J. Hafner, Mater. Sci. Eng. A **226-228**, 950 (1997).